Time and Space Distribution of Coseismic Slip of the 2011 Tohoku Earthquake as Inferred from Tsunami Waveform Data

Kenji Satake[1], Yushiro Fujii[2], Tomoya Harada[1] and Yuichi Namegaya[3]

Electronic Supplement

Estimated slip for each subfault at 0.5 min interval

http://iisee.kenken.go.jp/staff/fujii/BSSA_Tohoku/BSSA-D-12-00122R1-esupp.html

Corresponding author: Kenji Satake

Earthquake Research Institute, University of Tokyo

1-1-1 Yayoi, Bunkyo-ku, Tokyo 113-0032 Japan

satake@eri.u-tokyo.ac.jp

Revised on July 21, 2012

Final version September 26, 2012

Abstract A multiple time-window inversion of 53 high-sampling tsunami waveforms on ocean bottom pressure, GPS, coastal wave, and tide gauges shows a temporal and spatial slip distribution during the 2011 Tohoku earthquake. The fault rupture started near the hypocenter and propagated into both deep and shallow parts of the plate interface. Very large, approximately 25 m, slip off Miyagi on the deep part, at a location similar to the previous 869 Jogan earthquake model, was responsible for the initial rise of tsunami waveforms and the recorded tsunami inundation in Sendai and Ishinomaki plains. Huge slip, up to 69 m, occurred on the shallow part near the trench axis 3 min after the rupture initiation. This delayed shallow rupture extended for 400 km with more than 10 m slip, at a location similar to the 1896 Sanriku tsunami earthquake, and was responsible for the peak amplitudes of the tsunami waveforms and the maximum tsunami heights measured on the northern Sanriku coast, 100 km north of the largest slip. The average slip on the entire fault is 9.5 m and the total seismic moment is 4.2×10^{22} Nm (Mw = 9.0). The large horizontal displacement of seafloor slope is responsible for 20 to 40 % of tsunami amplitudes. The 2011 deep slip alone can reproduce the distribution of the 869 tsunami deposits, indicating that the 869 Jogan earthquake source could be similar to the 2011 earthquake at least in the deep plate interface. The large tsunami at the Fukushima nuclear power station is due to the combination of the deep and shallow slip, or triggering of shallow slip by the deep slip, which was not accounted in the previous tsunami hazard assessments.

Introduction

The 11 March 2011 Tohoku earthquake (the official name by the Japan Meteorological Agency (JMA) is "the 2011 off the Pacific coast of Tohoku earthquake") was the largest instrumentally recorded earthquake in Japan. The source parameters provided by JMA are as follows: the epicenter at 38° 06.2' N, 142° 51.6' E, depth 24 km, *M* 9.0, the origin time14:46:18.1 JST (GMT+ 9 hours). The focal mechanism shows a typical underthrust type (USGS W-phase mechanism: strike 193°, dip 14°, and slip angle 81°) associated with the subduction of the Pacific plate beneath the Tohoku region of Japan (Figure 1).

The 2011 Tohoku earthquake caused significant damage, including 16,278 fatalities and 2,994 missing in Tohoku and Kanto regions (The Fire and Disaster Management Agency, as of 13 March 2012). More than 90 % of fatalities were drowned by the tsunami. Large tsunami heights were measured along the Pacific coast of Tohoku with the maximum runup heights of nearly 40 m (Mori *et al.*, 2011; Tsuji *et al.*, 2011). The tsunami also attacked four nuclear power stations (NPS) located near the source area. Among them, the tsunami runup height at Fukushima Dai-ichi (Fukushima-1) NPS was approximately 15 m, much larger than the design height (6.1 m), leading to a loss of AC power to cool down the reactors, hydrogen explosions of three reactors, and release of radioactive materials.

For the slip distribution of the Tohoku earthquake, numerous models have been proposed by using teleseismic waves (*e.g.*, Ide *et al.*, 2011), strong-motion data (e.g., Yoshida *et al.*, 2011), land-based GPS data (*e.g.*, Ozawa *et al.*, 2011), tsunami data (*e.g.*, Fujii *et al.*, 2011), or combination of these (Simons *et al.*, 2011; Yokota *et al.*, 2011). A common feature of the source models from various types of data is huge (30 to 50 m) slip around the epicenter. However, the exact location of the maximum

slip varies from model to model. Some models using shorter period strong-motion data (*e.g.*, Yokota *et al.*, 2011) show the maximum peak at deep plate interface closer to the coast, while the results from GPS data tend to show the maximum slip at the shallow part near the trench axis (Figure 2).

The huge slip near the trench axis was detected and confirmed by various types of offshore geophysical measurements. The cable-type Ocean Bottom Pressure (OBP) gauges off Kamaishi (TM-1 and TM-2) recorded two-stage tsunamis: gradual water level rise of approximately 2 m followed by impulsive tsunami wave with another 3 m amplitude. The impulsive tsunami was modeled by huge seafloor displacement near the trench axis (Fujii *et al.*, 2011; Maeda *et al.*, 2011). Seafloor geodetic measurements using GPS and acoustic signals (GPS/A) or offline bottom pressure gauges detected large vertical (up to 5 m) and horizontal (up to 74 m) displacements (Ito *et al.*, 2011; Kido *et al.*, 2011; Sato *et al.*, 2011). Repeated multi narrow-beam sonar soundings also indicated that seafloor horizontally moved nearly 50 m near the trench axis (Fujiwara *et al.*, 2011).

The Pacific coasts of Tohoku have suffered from large tsunamis in the past. The 1896 Sanriku earthquake caused large (maximum runup height of ~40 m or more) tsunamis on the Sanriku coast with 22,000 casualties, although the seismic shaking was not very strong. Source of this "tsunami earthquake" (Kanamori, 1972) was located near the trench axis (Tanioka and Satake, 1996a; Tanioka and Seno, 2001). The 1933 Sanriku earthquake, a large outer-rise normal-fault earthquake (Kanamori, 1971), also caused large (maximum height of ~30 m) tsunami with approximately 3,000 casualties. The tsunami heights from these Sanriku earthquakes were smaller, less than a few meters, in Sendai plain (Sawai *et al.*, 2008a). However, the 869 Jogan earthquake produced large tsunami inundation up

91 to a few kilometers (Minoura and Nakaya, 1991), which was modeled by an
92 earthquake at deep plate interface (Satake *et al.*, 2008a; Namegaya *et al.*, 2010).
93 There are still unsolved issues related to the 2011 Tohoku earthquake and
94 tsunami. The first question is whether the slip increases or decreases toward the
95 trench axis. To answer this, the slip distribution along down-dip direction,
96 particularly near the trench axis, should be precisely estimated. The second
97 question is the cause of large,~100 km, latitude offset between the locations of the
98 largest slip and the maximum coastal tsunami height. The largest offshore slip near
99 the trench axis is located at around 38.5°N (Figure 2), whereas the measured
100 tsunami height distribution shows a peak near Miyako, around 39.6°N with the
101 maximum tsunami height of near 40 m (Mori *et al.*, 2011; Tsuji *et al.*, 2011). Another
102 question is whether the 869 Jogan earthquake source was similar to the 2011
103 earthquake. While previous studies on the 869 model (Satake *et al.*, 2008a;
104 Namegaya *et al.*, 2010) examined several types of earthquakes including the
105 interplate, outer-rise and tsunami earthquakes, they did not consider simultaneous
106 occurrence of these. Furthermore, what was the main cause of much larger tsunami
107 than the design heights at Fukushima NPSs ?
108 In this study, we extend the data and method of Fujii *et al.* (2011) to further
109 investigate the tsunami source of the 2011 Tohoku earthquake. Additional
110 tsunami waveforms recorded at GPS wave gauges and coastal tide and wave gauges
111 became available after the publication of our previous paper (Fujii *et al.*, 2011). For
112 the method, we introduce a multiple time-window analysis and estimate the spatial
113 and temporal distributions of tsunamigenic slip on the earthquake fault. We have
114 previously assumed that the slip occurred instantaneously, because the tsunami
115 data are usually not sensitive to rupture propagation even for a giant earthquake

with > 1,000 km rupture (Fujii and Satake, 2007). However, the 2011 tsunami was recorded on high-quality and high-sampling offshore gauges, and the waveforms recorded near the source region are sensitive to temporal change of slip. We assume 55 subfaults on the plate interface, by extending northwards of the subfaults in Fujii *et al.* (2011), and halving the width of the shallowest subfaults to better resolve the down-dip slip distribution near the trench axis. We also compute coastal tsunami heights, and tsunami inundation on Sendai and Ishinomaki plains using both the current bathymetry and the 869 topography data. We show that the large tsunami heights measured on the northern Sanriku coast can be explained by delayed shallow slip to the north of the largest slip. We also show that our source model can reproduce the 2011 tsunami inundation area and the distribution of the 869 tsunami deposits in those plains. We also summarize the design heights and 2011 tsunami heights at four NPS, and discuss the issues for future tsunami hazard assessment, based on our proposed model.

<Figures 1 , 2>

Tsunami Waveform Data

The 2011 tsunami was instrumentally recorded on various types of gauges. We used the tsunami waveforms recorded on 11 Ocean Bottom Pressure (OBP) gauges, 10 GPS wave gauges, and 32 coastal tide and wave gauges. The location, type of gauges, the water depth, the original sampling interval and the operating agencies of the gauges are summarized in Table 1. The OBP gauges are located in deep oceans. Seven OBP gauges ,2 by University of Tokyo and 5 by Japan Agency for Marine-Earth Science Technology (JAMSTEC), are connected to ocean bottom

cables, which allows high sampling rates (> 1 Hz). Data from 4 DART buoys are sent via acoustic wave and satellite, hence the sampling interval is typically 1 min. Ten GPS gauges and 7 wave gauges are a part of Nationwide Ocean Wave information network for Ports and HArbourS (NOWPHAS) system, which measures wave height at an interval of 5 s. A wave gauge is operated by Tokyo Electric Power Company (TEPCO) at Fukishima-1 NPS. Twenty-four coastal tide gauges are operated by various agencies such as JMA, Japan Coast Guard, or two power companies at NPS. Some of them stopped recording soon after the tsunami arrival, and only the initial portions of tsunami waveforms can be used for the analysis.

Most of the tsunami waveforms are recorded digitally. For the graphic sea-level data (Miyako, Ofunato, Ayukawa and Soma), we digitized the analog data and converted them into digital form with approximately 0.3 - 0.4 min interval.

Tidal components were removed from the original data. We first approximated the tidal component by fitting a polynomial function, and removed it from the original record.

<Table 1>

Method

Tsunami Computation

The tsunami source is divided into 55 subfaults to estimate the slip distribution (see Figure 2). The subfaults are basically 50 km long and 50 km wide, but the two columns of shallowest subfaults have a halved 25 km width. The northern four subfaults are added to the 40 subfaults of Fujii *et al.* (2011). The subfaults are located on the upper plane of subducting Pacific plate, following the

166 geometry inferred by Nakajima and Hasegawa (2006). The fault strike and slip
167 angles are adopted from USGS W-phase inversion result (strike 193º, slip angle 81º).
168 The top depths and the dip anglesare 0 and 3.5 km (beneath seafloor) and 8º for the
169 shallowest subfaults, 7 km and 10º for the third, 15.6 km and 12º for the fourth
170 subfaults from the trench, and 26 km and 16º for the deepest subfaults. Static
171 seafloor deformation is calculated for a rectangular fault model assuming an elastic
172 half-space (Okada, 1985). We also consider the effects of horizontal displacement in
173 regions of steep bathymetric slope (Tanioka and Satake, 1996b). As we discuss later,
174 the horizontal displacement contributes significantly to the tsunami amplitudes.

175 The linear shallow-water, or long-wave, equations and the equation of
176 continuity are numerically solved by using a finite-difference method (Satake, 1995;
177 Fujii and Satake, 2007), and are used as the Green's functions for the inversion. For
178 the tsunami waveforms at offshore OBP or GPS wave gauges, the nonlinear effect is
179 small, and the linear and nonlinear computations produce similar waveforms. The
180 nonlinear effect becomes important around coastal tide gauge stations, but we
181 confirmed, by comparing the nonlinear and linear computations, that they produce
182 similar arrival times and initial slopes. Although the computed peak amplitudes are
183 somewhat different, the peaks were not recorded at many nearby stations (*e.g.*,
184 Fritz *et al.*, 2012). For the computation of coastal tsunami heights, we use the
185 nonlinear equations. The Manning's roughness coefficient is set at 0.03 $m^{-1/3}$ s, and
186 total reflection on the coasts is assumed. For the inundation on Sendai and
187 Ishinomaki plains, we also include tsunami inundation on land, by introducing a
188 moving boundary condition (Satake *et al.*, 2008b).

189 We use different resolution bathymetric grids for calculating tsunami
190 waveforms, coastal tsunami heights and inundation. For the waveforms on DART

stations in the Pacific ocean, 2' interval grid for 125°-175°E and 15°-55°N is resampled from GEBCO_08 30"grid data. For the offshore stations around Japan, 30" interval grid of JTOPO30, provided by Marine Information Research Center (MIRC), is used for 128°-150°E and 25°-45°N. Time steps of 3 s and 1 s are used to satisfy the stability condition for the finite-difference method in the 2' and 30" grids, respectively. For the computations of coastal tsunami heights, in addition to JTOPO30 data, digital bathymetry charts (M7000 series) provided by MIRC are used. The grid size and computational time interval is 5" (approximately 150 m) and 0.2 s, respectively. For the inundation computations, topography data from Geospatial Information Authority of Japan (GSI) are also used for the land part. Variable grid sizes, the coarsest 2,025 m and finest 25 m, are adopted. The time interval of computation is 0.5 s, and the tsunami propagation during 3 hours after the earthquake is computed.

Multiple Time-Window Inversion

The basic assumption for the waveform inversion is a superposition principle, *i.e.* the recorded tsunami waveforms are assumed to be a linear superposition of computed tsunami waveforms from subfaults, or the Green's functions. In the previous tsunami waveform inversions (*e.g.*, Satake, 1987), rupture on a fault has been assumed to be instantaneous. For the 2004 Sumatra-Andaman earthquake with the fault length of 1,300 km, Fujii and Satake (2007) tried several rupture velocities, and concluded that the inversion result was insensitive to the choice of rupture velocity. This insensitivity may be due to the fact that most stations were far from the tsunami source and the sampling interval was typically 1 min or longer. For the 2011 Tohoku tsunami, in contrast, many

high-quality and high-sampling data were obtained within or near the tsunami source. In addition, the seismological analyses indicate that the source duration was more than 2 min (Ide *et al.*, 2011; Yoshida *et al.*, 2011). Hence, we consider temporal as well as spatial distribution of slip on subfaults, by introducing a multiple time-window analysis in the inversion.

For the multiple time-window inversion (Figure 3a), we first compute tsunami waveforms from each subfault, assuming a rise time of 30 s, then shift the computed tsunami waveforms, or the Green's functions, by a 30 s interval up to 120 s. Thus, for each station where the tsunami waveform was recorded, we have 5 Green's functions. The start time of the Green's function, or time windows, on subfault i is given as $t_i = m\,\Delta t + R_i/Vr$, where m is integer between 0 and 4, Δt is time interval (30 s), R_i is distance between the hypocenter and the edge of subfault i, and Vr is rupture velocity (2.0 km/s). While we tried and compared for other velocities (1.5, 2.5 km/s, and infinite velocity), the results were less sensitive to the choice of rupture velocity.

The total number of unknown parameters is 275, for the slip amounts of 55 subfaults times the five time windows. Because the observed tsunami waveforms were resampled at 12 s interval, the waveforms are computed at 12 s interval. The total number of data points used for the inversion is 15,335. For the inversion, we use the non-negative least square method (Lawson and Hanson, 1974) to avoid a negative slip. No smoothing or damping is used in the inversion.

We use different weights for different types of data. While the tsunami amplitudes are smaller at the deeper depth, they contain cleaner signal on the source free from coastal effects. The weights are 10 for the OBP gauge data, 5 for the GPS wave gauge data, 2 for the coastal wave gauge data, and 1 for the coastal

241 tide gauge data (see Table 1 for the sensor types). The water depths are more than
242 1,000 m at the OBP gauges, typically 200 m at the GPS gauges, a few tens of meter
243 at the coastal wave gauges, and several meters at the coastal tide gauges (Table 1).
244 Before we apply the multiple time-window inversion for the actual observed
245 data, we make resolution tests by using the synthetic data to examine the resolving
246 power, in both space and time. The synthetic tsunami waveforms are calculated
247 from a checker-board type slip distribution in space (10 m and 0 m in alternate
248 subfaults: Figure 3b) and variable start times of rupture (Figure 3c) with a constant
249 rise time (60 s, or over two time windows). We use the same time range and weights
250 as the observed data and make the inversion. The inversion result, the space-time
251 distribution of the slip, is almost the same as the assumed slip distribution (Figure
252 3c). Except for a few subfaults (*e.g.*, shallowest subfault 0D, where the estimated
253 slip slightly underestimates the input slip), the assumed slips are mostly recovered.
254 For the complementary slip distribution (Figure 3d), the results are even better. The
255 temporal changes of slip at some subfaults are slightly different from the assumed
256 ones, but both the rupture start time and the durations are almost perfectly
257 resolved.
258
259 **<Figure 3 >**
260
261 **Results of Inversion**
262 The time-space distribution of the 2011 Tohoku earthquake slip shows that
263 the rupture was not instantaneous but it took 1 to 4 min to reach the final slip on
264 each subfault (Table 2 and Figure 4). In the deep subfaults (2* to 4*), the final slip
265 was reached 3 min after the origin time of the earthquake. On subfault 2F near the

hypocenter, the slip was initially small (~ 11 m) for the first 1 min, but reached the final slip (~ 25 m) at 2.5 min. Such a two-stage slip increase is seen at the neighboring subfaults, and seems to propagate from the hypocenter toward the neighboring subfaults. On the northern shallow subfaults (0A, 0B and 0C), the slip started at 1.5 – 3 min and reached the final slip at 3 – 4 min.

The rupture propagation can be also seen in the snapshots of the slip distribution (Figure 5). The rupture started to propagate from the hypocenter, and reached the neighboring subfaults on deep plate interface within 2.5 min. This is similar to the duration of moment release (120 to 160 s) estimated from seismic waves (Ide *et al.*, 2011, Yoshida *et al.*, 2011; Yokota *et al.*, 2011). The large shallow slip then started to propagate toward the north and south along the trench axis at 3 min after the origin time.

The final slip distribution (Figure 6a) shows that the largest slip was 69 m located on the shallowest subfault (0F) east of the hypocenter. This largest slip is similar to estimated slip of ~ 70 m on the plate interface (Ito *et al.*, 2011). Huge (>30 m) slip occurred on the shallowest subfaults (0C through 0G) over a length of 250 km. Large (> 10 m) slip is extended on shallow subfaults from 0A through 0H along the trench axis, forming the total length of 400 km. This is approximately twice as long as the 1896 Sanriku tsunami earthquake fault (200 km, Tanioka and Seno, 2001).

We also estimated the slip distribution for a 44-subfault model, which assumed the same subfault size (50 km x 50 km) for the entire source region (Figure 6b). While we confirmed that our 55-subfault model has enough resolution for the shallow subfaults, the 44-subfault model provides slip distribution with uniform spatial resolution. The 44-subfault model also shows largest slip at the shallowest

291 subfaults, although the slip values are averaged resulting in a smaller maximum
292 slip amount (~ 38 m).

293 The slip on deep plate interface reaches at maximum around 25 m on
294 subfaults near the hypocenter (2E, 2F and 3F). The large (> 10 m) slip is located on
295 200 km, 150 km and 50 km long regions from shallow to deepest subfaults. The slip
296 distribution on deep subfaults is basically the same for the 44-subfault and
297 55-subfault models.

298 The slip distribution pattern is basically similar to that estimated from
299 GPS data (Figure 2b), but the maximum slip is located at the shallowest part. In
300 addition, the shallow slip extended north compared with the GPS results. On the
301 contrary, the maximum slip from strong-motion data is located at the deep subfaults
302 (Figure 2a). This may be either because the offshore shallow slip did not generate
303 the short-period energy or because the short-period energy from the shallow
304 subfaults near the epicenter attenuated during the propagation.

305 The computed tsunami waveforms from the slip distribution model
306 generally agree with the observed ones at most stations (Figures 7). The observed
307 tsunami waveforms at OBP and GPS wave gauges (Figure 7a) are well reproduced.
308 The maximum computed amplitudes of the sharp peak are larger at some stations
309 (Iwate N and S) but smaller at others (Iwate M). A comparison with the results of
310 Fujii *et al.* (2011) indicates that the computed waveform at the northern GPS wave
311 gauge (Iwate N) is much closer to the observations. At the coastal wave and tide
312 gauges (Figures 7b and c), the waveform match is slightly worse, because the
313 coastal topography around the gauges and nonlinear effects are not included in the
314 computations.

315 The average slip on the 55 subfaults is computed as 9.5 m. The seismic

316 moment is calculated as 4.2 x 10^{22} Nm (Mw = 9.0), assuming an average rigidity of 4
317 x 10^{10} N/m^2 for the entire subfaults. For the shallow subfaults, the average slip is
318 18.6 m, and the seismic moment is 2.1 x 10^{22} Nm (Mw = 8.8). For the deep subfaults,
319 they are 6.4 m and 2.1 x 10^{22} Nm (Mw = 8.8), respectively. If we separate the slip
320 distribution into shallow and deep subfaults, it can be considered that a great
321 earthquake (Mw 8.8) on the deep subfaults triggered another one (Mw 8.8) on the
322 shallow subfaults near the trench axis, as will be discussed in later section.
323
324 **<Table 2 and Figures 4, 5, 6, 7a, 7b, 7c>**
325
326 **Seafloor Deformation and Effects of Horizontal Displacement**
327 The Tohoku earthquake produced large seafloor and land deformations.
328 The largest vertical displacement measured on the seafloor was 5 m uplift (Ito *et al.*,
329 2011; Kido *et al.*, 2011; Sato *et al.*, 2011), while the largest coastal subsidence was
330 ~1.2 m (Ozawa *et al.*, 2011). The maximum vertical seafloor displacement computed
331 from our slip distribution model is more than 10 m above the shallowest subfault
332 with the largest slip (0F; Figure 8a). At the GPS/A measurement locations (Sato *et*
333 *al.*, 2011; Figure 8a), the computed vertical displacements are larger than the
334 measured ones at four locations, and in an opposite direction at one location. The
335 maximum computed subsidence is >1.5 m offshore, and > 1.0 m along the coast.
336 The horizontal displacement was larger. The computed horizontal
337 displacements at the GPS/A stations are slightly smaller than the measured ones
338 except at one location (Figure 8a). Near the trench axis, huge (50 to 70 m) horizontal
339 displacements were measured (Ito *et al.*, 2011; Fujiwara *et al.*, 2011). Very large
340 horizontal displacements affect the tsunami generation, if the ocean bottom is not

341 flat. Tanioka and Satake (1996b) showed that the horizontal displacement near a
342 trench axis can amplify the tsunami amplitude by 30 % because of the steep seafloor
343 slope. While we already accounted for the effects in this study, they are not usually
344 incorporated in other tsunami computations, hence it would be interesting to
345 examine the effects.

346 The vertical seafloor deformation computed from the final slip distribution
347 (Table 2 and Figure 6a) are compared with and without including the horizontal
348 movements (Figure 8). Near the trench axis, both horizontal displacement and
349 ocean bottom slope are large, hence the effective vertical displacement becomes
350 larger. It should be also noted that the horizontal displacement adds shorter
351 wavelength components of initial sea surface displacement.

352 The computed tsunami waveforms including the horizontal component are
353 larger than those from vertical component alone. At the OBP and GPS wave gauge
354 stations in or near the source region (Figure 9), the largest amplitudes are larger by
355 30 to 60 % if the effects of horizontal displacement are included. In other words,
356 approximately 20 to 40 % of the largest tsunami amplitude was due to the effects of
357 horizontal component, rather than the vertical component, of seafloor displacement.
358 The difference is more visible at the first peak with a short period (several min).
359 This is because the slope is steeper near the trench axis where the short period
360 tsunami wave was generated.

361

362 **<Figures 8 and 9>**

363

364 **Effects of Delayed Slip**

365 The temporal and spatial slip distribution of the 2011 Tohoku earthquake

366 was estimated through a multiple time-window inversion of the tsunami waveforms
367 with high-sampling rates in or around the tsunami source. The result indicated that
368 the tsunamigenic slip was not instantaneous but the duration was ~ 2.5 min. In
369 addition, the shallow slip was delayed by ~ 3 min. In order to examine the effect of
370 such delayed rupture, we compute the tsunami waveforms for the different cases:
371 one with the delayed slip and the other assuming an instantaneous slip. For the
372 delayed slip case, we first compute the slip on each subfault in 30 s increments (as
373 shown in Figure 5) by interpolation of the inversion results (Figure 4 and Table 2),
374 then use it as initial conditions of tsunami propagation (Table S1: available in the
375 electronic supplement to this article). For the instantaneous case, we assume that
376 the final slip distribution is achieved in the first 30 s. Figure 10 shows that the
377 computed tsunami waveforms for the delayed rupture are similar to the observed
378 waveforms. The computed waveforms in Figures 9 and 10 are calculated in different
379 ways, based on the results in Tables 2 and S1 (available in the electronic
380 supplement to this article), respectively. Nevertheless, they are almost identical. On
381 the contrary, the tsunami computed from an instantaneous slip arrives earlier with
382 larger amplitudes than the observed at all the stations. The difference becomes
383 smaller at distant stations (Fukushima) and almost invisible at other farther
384 stations (not shown in Figure).

385 The delayed slip also affects the coastal tsunami heights. We compute the
386 coastal tsunami heights using the 5" grid bathymetry from the two different initial
387 conditions: the delayed slip and the instantaneous slip. Figure 11 shows that the
388 tsunami heights calculated from an instantaneous slip show a uniform distribution,
389 within a 10 to 30 m range, along the Sanriku coast (between 38.5° and 40°N), and
390 they generally overestimate the observed heights, particularly on the southern

391 Sanriku coast (between 38.5° and 39°N). The computed coastal tsunami heights
392 from the delayed slip are larger to the north (with a peak at around 40°N), and the
393 maximum values gradually decrease toward the south. The observed heights also
394 show the maximum values on the northern Sanriku coasts, and the observed and
395 computed heights from the delayed slip are roughly similar. The 100 km offset
396 between the maximum slip on fault and the maximum tsunami height was resolved
397 by introducing the delayed large slips (up to ~36 m) at around 3.5 min (subfaults 0A,
398 0B and 0C). The computed heights on the southern Ibaraki and Chiba coasts from
399 both cases are similar to each other, and also similar to the observed heights.
400
401 **<Figures 10 and 11>**
402
403 **Deep and Shallow Slips**
404 The estimated slip distribution (Figure 6a and Table 2) can be decomposed
405 into deep slip (on subfaults 2*, 3* and 4*) and shallow slip (on subfaults 0* and 1*).
406 The location of the deep slip on a plate interface is similar to the
407 previously-proposed 869 Jogan earthquake model (Satake *et al.*, 2008a; Namegaya
408 *et al.*, 2010), and the location of the shallow slip with respect to the trench axis is
409 similar to the proposed model of the 1896 Sanriku earthquake (Tanioka and Satake,
410 1996a; Tanioka and Seno, 2001). The large slip near the trench axis, a typical
411 feature of “tsunami earthquakes”, is responsible for the large coastal tsunami
412 heights along the Sanriku coast. This is evident in Figure 12a, where the tsunami
413 waveforms are computed separately from the deep and shallow slips. The tsunamis
414 computed from the deep subfaults arrive earlier, and reproduce gradual sea level
415 rises. The tsunami waveforms computed from the shallow slip show later arrivals

and reproduce the large impulsive tsunamis. The two-step tsunami waveforms, recorded at some offshore stations such as TM-1, TM-2 and Iwate-S, can be reproduced by combination of deep and shallow slips, as pointed out by Fujii *et al.* (2011).

Large tsunami inundations (> 3 km) in Sendai and Ishinomaki plains are due to deep slip on the plate interface. We computed tsunami inundation areas in these plains from three models: the 2011 slip model, the deep slip model and the shallow model (Figure 13). The computed inundation areas from the deep slip are similar to the 2011 slip model, and also similar to the actual tsunami inundation areas in 2011 estimated by GSI (Nakajima and Koarai, 2011). On the other hand, the tsunami inundation area computed from only the shallow subfaults is much smaller than the actual one. This indicates that the large tsunami inundation was due to the deep slip, not the huge shallow slip near the trench axis. The huge offshore slip produces large seafloor deformation with a short wavelength. The resultant tsunami is dominant in short periods, hence cannot inundate far overland. On the other hand, a slip on the deep fault produces seafloor deformation with a longer wavelength, hence the period of tsunami become longer, and can penetrate deeply inland (Satake *et al.*, 2008b).

<Figures 12 and 13>

Was the Jogan Earthquake Similar to the 2011 Earthquake ?

For the 869 Jogan tsunami, Satake *et al.* (2008a) and Namegaya *et al.* (2010) proposed a fault model with 200 km length and 100 km width, by examining several fault models such as interplate, outer-rise fault or “tsunami earthquake”

441 model. The question arises whether the 869 Jogan earthquake was similar to the
442 2011 Tohoku earthquake. In order to provide an answer, we compute tsunami
443 inundation using the reconstructed bathymetry and topography at the time of the
444 869 earthquake, as carried out by Satake *et al.* (2008a) and Namegaya *et al.* (2010).
445 The coastal geological studies indicate that the 869 coast lines were located at 1 to
446 1.5 km inland from the current coast, and the tsunami deposits were distributed 1
447 to 3 km from the estimated coast lines (Sawai *et al.*, 2007; Shishikura *et al.*, 2007;
448 Sawai *et al.*, 2008b). We then compare the computed tsunami inundation areas with
449 the distribution of the 869 tsunami deposits as revealed by the above geological
450 studies.

451 The results (Figure 14) show that the computed inundation areas from the
452 2011 slip model and the deep slip are similar and both roughly reproduced the
453 distribution of the tsunami deposits, whereas the computed inundation area from
454 the shallow slip of the 2011 source is much smaller. The results for the 869
455 topography are basically similar to the results for the current topography in the
456 previous section. The inundation area computed from the shallow slip cannot
457 reproduce the distribution of the 869 tsunami deposits. This confirms that the 869
458 Jogan earthquake source requires deep slip, as proposed by Satake *et al.* (2008a)
459 and Namegaya *et al.* (2010). While the slip amounts and the seismic moment on the
460 deep faults estimated in the above studies were up to 7 m and Mw = 8.4, they were
461 the minimum estimate to match the computed inundation area with the
462 distribution of tsunami deposits. The current comparison indicates that the 869
463 Jogan earthquake possibly had a similarly large (~25 m) slip with the 2011 slip on
464 the deep plate interface, and the moment magnitude of the 869 earthquake could be
465 as large as Mw = 8.8. However, we cannot judge, from the tsunami deposits in

Sendai and Ishinomaki plains, whether or not such a deep slip also triggered the shallow slip at the time of the Jogan earthquake in 869 and the seismic moment was similar to the 2011 earthquake (Mw = 9.0).

<Figure 14>

Tsunami Accidents and Hazard Assessment at Nuclear Power Stations

The 2011 Tohoku earthquake caused tsunami damage at the Fukushima Dai-ichi (Fukushima-1) NPS, which led to one of the worst nuclear accidents. Besides Fukushima-1, three other NPSs are located near the source area of the 2011 Tohoku earthquake (Figure 6b). At these NPSs, the strong ground shaking automatically shut down the reactors, and the diesel generators started to cool down the reactors. At Fukushima-1 and Fukushima-2 (Dai-ni) stations, the tsunami flooded and damaged the diesel generators. Because the strong ground shaking also damaged the external power supply system at Fukushima-1, it lost all the power supplies, leading to the station black out. Thus the Fukushima-1 station failed to cool down the reactors, causing melt-down, hydrogen explosions of three reactors, and release of radioactive materials.

In this section, we first briefly review the design tsunami heights and the actual tsunami heights at these NPSs. The design tsunami heights for the Japanese NPSs were set by a deterministic method, based on the past large earthquakes and by making parameter studies (Yanagisawa *et al.*, 2007). For the Fukushima-1 and -2 NPSs, the 1938 Shioya-oki earthquakes, a series of large earthquakes with M = 7.4 to 7.8 (Abe, 1977), were used for the parameter studies. By varying several fault parameters of these earthquakes, the design tsunami, which yields the maximum

491 tsunami height at NPS, was selected. The design tsunami heights were 6.1 m and
492 5.2 m above local datum (Onahama Peil or OP) at Fukushima-1 and -2 NPSs,
493 respectively. The site levels, on which critical facilities such as the reactor and
494 turbine buildings are located, are 10-13 m above OP at Fukushima-1 and 12 m
495 above OP at Fukushima-2 NPSs. The 2011 tsunami with the runup heights of 15.5
496 m and 14.5 m above OP, respectively at Fukushima-1 and -2 NPSs, flooded and
497 stopped the diesel generators. At Onagawa NPS, the design height was 13 m above
498 local datum (Onagawa Peil, also OP but different from Onahama Peil), based on the
499 1896 Sanriku tsunami, and the site level was 14.8 m above OP before coseismic
500 subsidence of ~1 m during the 2011 earthquake. The 2011 tsunami was 13 m high
501 above OP and did not reach the main facilities, while the tsunami inundated the
502 basement of the reactor building through a seawater pump conduit. At Tokai NPS,
503 the design tsunami height was 6.6 m above local datum (Hitachi Peil or HP) based
504 on the 1677 Boso earthquake, and the site level was 8.9 m above HP. The 2011
505 tsunami height was 6.2 m above HP, and caused slight damage on seawater pump.
506 We compute tsunami waveforms from the 2011 slip model, deep and
507 shallow slips at the four NPSs (Figure 15). The output points in our computations
508 are on the coast, not on the NPS sites, hence the tsunami heights on the NPS sites
509 would be different. Nevertheless, we can compare and examine the basic features
510 related to the tsunami source. The tsunami amplitudes from the deep and shallow
511 sources are approximately 7 m and 4 m, respectively, at both Fukushima-1 and
512 Fukushima-2. However, the tsunami amplitude from the 2011 slip model, or
513 composite of the deep and shallow slips, show a large second peak with
514 approximately 9 m at Fukushima-1 and 7 m at Fukushima-2. This indicates that
515 the simultaneous arrival of tsunamis from the deep slip and the delayed shallow

slip amplified the tsunami heights, and caused the disastrous tsunami at Fukushima-1 NPS. The TEPCO also estimated, before 2011, that tsunami from a shallow slip, similar to the 1896 Sanriku tsunami earthquake, would be as large as 15.7 m, and from a deep slip (the 869 Jogan earthquake) model would produce 7.9 to 8.9 m at Fukushima-1 site.

At Onagawa NPS, the peak amplitudes from the deep slip and negative trough of the shallow slip arrived at around the same time, making the composite amplitude smaller than those of each source. In other words, if the deep and shallow slips occurred separately, the tsunami at this site could have been larger than the observed, and may have caused a similar accident at this site.

A probabilistic tsunami hazard analyses, including other types of sources, have been proposed (Sakai *et al.*, 2006; Annaka *et al.*, 2007). The epistemic uncertainty, such as whether a "tsunami earthquake" would occur along the trench axis off Fukushima, was treated as a branch of a logic-tree. Then a hazard curve, or annual probability of exceedance versus tsunami heights, was constructed by integration over aleatory uncertainty. While the deep slip (Jogan earthquake type) and shallow slip ("tsunami earthquake" type) were considered in the logic trees, the simultaneous or delayed occurrence of two types of earthquakes was not considered.

The tsunami heights from the 2011 slip model, a combination of the deep and shallow slip, was larger at Fukushima NPSs than deep or shallow slip alone. However, the tsunami heights would be larger at Onagawa NPS from separate sources. For future tsunami hazard assessments, in addition to characterizing the 2011 source as a gigantic earthquake, it would be necessary to decompose the 2011 source into two types, deep and shallow slips, and treating them separately.

<Figure 15>

Conclusions

We expanded the tsunami waveform inversion of Fujii *et al.* (2011) by using a larger number (53) of tsunami waveforms recorded at ocean bottom pressure gauges, GPS wave gauges, and coastal wave and tide gauges (Figure 1 and Table 1), as well as by extending the subfaults to the north and by halving the width of shallow subfaults near the trench axis (Figure 2). We also introduced a multiple time-window inversion to allow temporal change of slip. The checker-board tests indicated that the temporal change of slip and the exact location of shallow slip can be well resolved (Figure 3). The inversion result (Figures 4 and 5) shows that rupture started near the hypocenter and the very large (> 25 m) slip occurred on the deep plate interface near the hypocenter within ~2.5 min, then huge (up to 69 m) slip occurred along the trench axis at 3 min after the origin time. This huge shallow slip then propagated to the north with > 20 m slip occurred at around 4 min after the rupture initiation. The final slip distribution (Figure 6 and Table 2) shows that the slip increases toward the trench axis.

The average slip on 550 km long and 200 km wide fault is 9.5 m, and the total seismic moment is estimated as 4.2×10^{22} Nm (Mw = 9.0). The delayed rupture produced better fit to the observed tsunami waveforms (Figures 7), particularly in the northern offshore stations within the tsunami source region. The computed seafloor deformation roughly matched to the vertical and horizontal displacements measured offshore (Figure 8). Examination of large horizontal displacement on seafloor slope (Tanioka and Satake, 1996b) shows that the sea surface uplift and tsunami amplitudes are approximately 30 to 60 % larger if we include these effects

566 (Figure 9). The delayed rupture better reproduced the observed tsunami waveforms
567 than the instantaneous rupture (Figure 10).

568 The huge slip on the shallow parts of the plate interface near the trench
569 axis was similar to the proposed model of the 1896 Sanriku "tsunami earthquake"
570 (Tanioka and Satake, 1996a; Tanioka and Seno, 2001), but the slip was larger (up to
571 69 m) and longer (400 km for > 10 m slip). The delayed slip along the trench axis
572 was responsible for the largest tsunami heights measured along the northern
573 Sanriku coast, ~100 km north of the largest slip (Figure 11), and the peaks of the
574 observed tsunami waveforms (Figure 12). However, the tsunami from the huge
575 shallow slip do not inundate far into Sendai or Ishinomaki plains (Figures 13 and
576 14), and we cannot judge whether or not such a huge shallow slip near the trench
577 axis occurred during the 869 Jogan earthquake.

578 The very large (~25 m) slip off Miyagi on the deep plate interface was
579 similar to the previously proposed model of the 869 Jogan earthquake (Satake *et al.*,
580 2008a; Namegaya *et al.*, 2010), and reproduced the initial rise of observed tsunami
581 waveforms (Figure 12) as well as the large tsunami inundation in Sendai and
582 Ishinomaki plains (Figure 13). The computed inundation areas on the 869
583 topography also cover the distribution of the 869 tsunami deposits (Figure 14),
584 suggesting that the 869 tsunami source was similar to the deep slip of the 2011
585 source.

586 One of the reasons for the large tsunami at Fukushima NPPs is the
587 combination of the shallow slip ("tsunami earthquake" type) and the deep slip
588 (Jogan earthquake type). Such simultaneous rupture, or triggering of shallow slip
589 by the deep slip, which amplifies or reduces the coastal tsunami heights, was not
590 considered in the previous tsunami hazard assessments.

Data and Resources

The tsunami waveforms used in this study were recorded and provided by Earthquake Research Institute (ERI) of the University of Tokyo, Japan Meteorological Agency (JMA), Japan Coast Guard (JCG), Ports and Harbors Bureau under the Ministry of Land, Infrastructure, Transport and Tourism (MLIT), Port and Airport Research Institute (PARI), Japan Agency for Marine-Earth Science and Technology (JMASTEC), Tohoku Electric Power Company, Tokyo Electric Power Company, Japan Atomic Power Company, and National Oceanic and Atmospheric Administration (NOAA) of USA. The GPS wave gauge data are available from Nationwide Ocean Wave information network for Ports and HArbourS (NOWPHAS) website http://nowphas.mlit.go.jp/nowphasdata/sub301.htm, tide gauge data from JCG are available at http://near-goos1.jodc.go.jp/index.html, and the DART data are available at http://www.ndbc.noaa.gov/dart.shtml (All the websites were last accessed on March 31, 2012). Other data are available from the recoding agencies upon request.

Acknowledgments

We thank Takeo Ishibe and Hermann Fritz for critically reading the manuscript and providing valuable comments on the manuscript. We also thank Eric Geist (the guest editor), Stefano Lorito and an anonymous reviewer, who provided us valuable comments. Most figures were generated using the Generic Mapping Tools (Wessel and Smith, 1998). This research was partially supported by Grants-in-Aid for Scientific Research (B) (No. 21310113), Ministry of Education, Culture, Sports, Science and Technology (MEXT).

616

617 **References**

618 Abe, K. (1977). Tectonic implications of the large Shioya-oki earthquakes of 1938.
619 *Tectonophysics*, **41**, 269-289.

620 Annaka, T., K. Satake, T. Sakakiyama, K. Yanagisawa, and N. Shuto (2007).
621 Logic-tree approeach for probabilistic tsunami hazard analysis and its
622 applications to the Japanese coasts. *Pure Appl. Geophys.*, **164**, 577-592.

623 Fritz, H.M., D.A. Phillips, A. Okayasu, T. Shimozono, H. Liu, F. Mohammed, V.
624 Skanavis, C.E. Synolakis, and T. Takahashi (2012). 2011 Japan tsunami
625 current velocity measurements from survivor videos at Kesennuma Bay
626 using LiDAR, *Geophys. Res. Lett.,* 39, L00G23.

627 Fujii, Y. and K. Satake (2007). Tsunami Source of the 2004 Sumatra-Andaman
628 Earthquake inferred from Tide Gauge and Satellite Data. *Bull. Seism. Soc.*
629 *Am.*, **97**(1A), S192-S207.

630 Fujii, Y., K. Satake, S. Sakai, M. Shinohara, and T. Kanazawa (2011). Tsunami
631 source of the 2011 off the Pacific coast of Tohoku Earthquake. *Earth Planets*
632 *Space*, **63**(7), 815-820.

633 Fujiwara, T., S. Kodaira, T. No, Y. Kaiho, N. Takahashi, and Y. Kaneda (2011). The
634 2011 Tohoku-Oki earthquake: displacement reaching the trench axis.
635 *Science*, **334**(6060), 1240-1240.

636 Geospatial Information Authority of Japan (2011). Crustal movements in the
637 Tohoku District (in Japanese). *Rep. Coord.Comm. Earthq. Pred., Japan*, **86**,
638 185-272.

639 Ide, S., A. Baltay, and G.C. Beroza (2011). Shallow dynamic overshoot and energetic
640 deep rupture in the 2011 M(w) 9.0 Tohoku-Oki earthquake. *Science*,

641 **332**(6036), 1426-1429.
642 Ito, Y., T. Tsuji, Y. Osada, M. Kido, D. Inazu, Y. Hayashi, H. Tsushima, R. Hino, and
643 H. Fujimoto (2011). Frontal wedge defromation near the source region of the
644 2011 Tohoku-oki earthquake. *Geophys. Res. Lett.*, **38**, L00G05:
645 doi:10.1029/2011GL048355.
646 Kanamori, H. (1971). Seismological evidence for a lithospheric normal faulting –
647 The Sanriku earthquake of 1933. *Phys. Earth Planet. Inter.*, **4**, 289-300.
648 Kanamori, H. (1972). Mechanism of tsunami earthquake. *Phys. Earth Planet. Inter.*,
649 **6**, 346-359.
650 Kido, M., Y. Osada, H. Fujimoto, R. Hino, and Y. Ito (2011). Trench-normal variation
651 in observed seafloor displacements associated with the 2011 Tohoku-Oki
652 earthquake. *Geophys. Res. Lett.*, **38**, L24303, doi:10.1029/2011GL050057.
653 Lawson, C. L. and R.J. Hanson (1974). *Solving least squares problems*. Englewood
654 Cliffs, N.J., Prentice -Hall, Inc.
655 Maeda, T., T. Furumura, S. Sakai and M. Shinohara (2011). Significant tsunami
656 observed at ocean-bottom pressure gauges during the 2011 off the Pacific
657 coast of Tohoku Earthquake. *Earth Planets Space*, **63**(7), 803-808.
658 Minoura, K. and S. Nakaya (1991). Traces of tsunami preserved in inter-tidal
659 lacustrine and marsh deposits: some examples from northeast Japan. *J.*
660 *Geology*, **99**, 265-287.
661 Mori, N., T. Takahashi, T. Yasuda, and H. Yanagisawa (2011). Survey of 2011
662 Tohoku earthquake tsunami inundation and run-up. *Geophys. Res. Lett.*, **38,**
663 L00G14, doi:10.1029/2011GL049210.
664 Nakajima, J. and A. Hasegawa (2006). Anomalous low-velocity zone and linear
665 alignment of seismicity along it in the subducted Pacific slab beneath Kanto,

666 Japan: Reactivation of subducted fracture zone? *Geophys. Res. Lett.*, **33,**
667 L16309, doi: 10.1029/2006GL026773.
668 Nakajima, H. and M. Koarai (2011). Assessment of Tsunami Flood Situation from
669 the Great East Japan Earthquake. *Bull. Geospatial Information Authority*
670 *of Japan*, **59**, 55-66.
671 Namegaya, Y., K. Satake and S. Yamaki (2010). Numerical simulation of the AD 869
672 Jogan tsunami in Ishinomaki and Sendai plains and Ukedo river-mouth
673 lowland (in Japanese with Englsih abstract). *Ann. Rep. Active Fault*
674 *Paleoearthquake Res.*, **10**, 1-21.
675 Okada, Y. (1985). Surface deformation due to shear and tensile faults in a half-space.
676 *Bull. Seism. Soc. Am.*, **75**(4), 1135-1154.
677 Ozawa, S., T. Nishimura, H. Suito, T. Kobayashi, M.Tobita, and T. Imakiire (2011).
678 Coseismic and postseismic slip of the 2011 magnitude-9 Tohoku-Oki
679 earthquake. *Nature*, **475**(7356), 373-376.
680 Sakai, T., T. Takeda, H. Soraoka, K. Yanagisawa, and T. Annaka (2006).
681 Development of a probabilistic tsunami hazard analysis in Japan.
682 *Proceedings of ICONE14 (14th International Conference on Nuclear*
683 *Engineering)*, Miami, Florida, USA, ASME.
684 Satake, K. (1987). Inversion of tsunami waveforms for the estimation of a fault
685 Heterogeneity - method and numerical experiments. *J. Phys. Earth*, **35**(3),
686 241-254.
687 Satake, K. (1995). Linear and nonlinear computations of the 1992 Nicaragua
688 earthquake tsunami. *Pure Appl. Geophys.*, **144**(3-4), 455-470.
689 Satake, K., Y. Namegaya, and S. Yamaki (2008a). Numerical simulation of the AD
690 869 Jogan tsunami in Ishinomaki and Sendai plains (in Japanese with

691 Englsih abstract). *Ann. Rep. Active Fault Paleoearthquake Res.*, **8**, 71-89.
692 Satake, K., F. Nanayama and S. Yamaki (2008b). Fault models of unusual tsunami
693 in the 17th century along the Kuril trench. *Earth Planets Space*, **60**(9),
694 925-935.
695 Sato, M., T. Ishikawa, N. Ujihara, S. Yoshida, M. Fujita, M. Mochizuki, and A.
696 Asada (2011). Displacement above the hypocenter of the 2011 Tohoku-Oki
697 earthquake. *Science*, **332**(6036), 1395-1395.
698 Sawai, Y., M. Shishikura, Y. Okamura, K. Takada, T. Matsu'ura, T.T. Aung, J.
699 Kamotsubara, Y. Fujii, O. Fujiwara, K. Satake, T. Kamataki, and N. Sato
700 (2007). A study on plaeotsunami using handy geoslicer in Sendai plain
701 (Sendai, Natori, Iwanuma, Watari and Yamamoto), Miyagi, Japan (in
702 Japanese with English abstract). *Ann. Rep. Active Fault Paleoearthquake*
703 *Res.*, **7**, 47-80.
704 Sawai, Y., Y. Fujii, O. Fujiwara, T. Kamataki, J. Komatsubara, Y. Okamura, K.
705 Satake, and M. Shishikura (2008a). Marine incursions of the past 1500
706 years and evidence of tsunamis at Suijin-numa, a coastal lake facing the
707 Japan Trench. *Holocene*, **18**(4), 517-528.
708 Sawai, Y., M. Shishikura, and J. Komatsubara (2008b). A study on paleotsunami
709 using hand corer in Sendai Plain (Sendai City, Natori City, Iwanuma City,
710 Watari Town, Yamamoto Town), Miyagi, Japan (in Japanese with Englsih
711 Abstract). *Ann. Rep. Active Fault Paleoearthquake Res.* , **8**, 17-70.
712 Sella, G. F., T.H. Dixon, and A.L. Mao (2002). REVEL: A model for Recent plate
713 velocities from space geodesy. *J. Geophys. Res.*, **107**(B4).
714 Shishikura, M., Y. Sawai, Y. Okamura, J. Komatsubara, T.T. Aung, T. Ishiyama, O.
715 Fujiwara, and S. Fujino (2007). Age and distribution of tsunami deposit in

716 the Ishinomaki plain, northeastern Japan (in Japanese with English
717 abstract). *Ann. Rep. Active Fault Paleoearthquake Res.*, **7**, 31-46.
718 Simons, M., S.E. Minson, A. Sladen, F. Ortega, J.L. Jiang, S.E. Owen, L.S. Meng, J.P.
719 Ampuero, S.J. Wei, R.S. Chu, D.V. Helmberger, H. Kanamori, E. Hetland,
720 A.W. Moore, and F.H. Webb (2011). The 2011 Magnitude 9.0 Tohoku-Oki
721 earthquake: Mosaicking the megathrust from seconds to centuries. *Science*,
722 **332**(6036), 1421-1425.
723 Tanioka, Y. and K. Satake (1996a). Fault parameters of the 1896 Sanriku tsunami
724 earthquake estimated from numerical modeling. *Geophys. Res. Lett.*, **23**,
725 1549-1552.
726 Tanioka, Y. and K. Satake (1996b). Tsunami generation by horizontal displacement
727 of ocean bottom. *Geophys. Res. Lett.*, **23**(8), 861-864.
728 Tanioka, Y. and T. Seno (2001). Sediment effect on tsunami generation of the 1896
729 Sanriku tsunami earthquake. *Geophys. Res. Lett.*, **28**(17), 3389-3392.
730 Tsuji, Y., K. Satake, T. Ishibe, S. Kusumoto, T. Harada, A. Nishiyama, H.Y. Kim, T.
731 Ueno, S. Murotani, S. Oki, M. Sugimoto, J. Tomari, M. Heidarzadeh, S.
732 Watada, K. Imai, B.H. Choi, S.B. Yoon, J.S. Bae, K.O. Kim, and H.W. Kim
733 (2011). Field Surveys of Tsunami Heights from the 2011 off the Pacific Coast
734 of Tohoku, Japan Earthquake (in Japanese with English abstract). *Bull.*
735 *Earthq. Res. Inst. Univ. Tokyo*, **86**, 29-279.
736 Wessel, P. and W.H.F. Smith (1998). New, improved version of the Generic Mapping
737 Tools released. *EOS Trans. AGU*, **79**, 579.
738 Yanagisawa, K., F. Imamura, T. Sakakiyama, T. Annaka, T. Takeda, and N. Shuto
739 (2007). Tsunami assessment for risk management at nuclear power facilities
740 in Japan. *Pure Appl. Geophys.*, **164**, 565-576.

Yokota, Y., K. Koketsu, Y. Fujii, K. Satake, S. Sakai, M. Shinohara, and T. Kanazawa (2011). Joint inversion of strong motion, teleseismic, geodetic, and tsunami datasets for the rupture process of the 2011 Tohoku earthquake. *Geophys. Res. Lett.*, **38**.

Yoshida, Y., H. Ueno, D. Muto, and S. Aoki (2011). Source process of the 2011 off the Pacific coast of Tohoku Earthquake with the combination of teleseismic and strong motion data. *Earth Planets Space*, **63**(7), 565-569.

Authors' affiliation, addresses

Earthquake Research Institute, University of Tokyo
1-1-1 Yayoi, Bunkyo-ku, Tokyo 113-0032 Japan
satake@eri.u-toko.ac.jp
haratomo@eri.u-toko.ac.jp
(K.S., T.H.)

International Institute of Seismology and Earthquake Engineering,
Building Research Institute,
1 Tachihara, Tsukuba, Ibaraki 305-0802 Japan
fujii@kenken.go.jp
(Y.F.)

Active Fault and Earthquake Research Center
Geological Survey of Japan, AIST
1-1-1 Higashi, Tsukuba, Ibaraki 305-8567 Japan
yuichi.namegaya@aist.go.jp
(Y.N.)

765 Table 1. List of tsunami gauge stations used in this study

766

Station	Type*	Lat.(º N)	Lon.(º E)	Water depth (m) †	Record sampling‡	Agencies§
TM-1	OBP	39.23119	142.76835	1,618	0.1 s	ERI
TM-2	OBP	39.24889	142.44115	1,013	0.1 s	ERI
KPG1	OBP	41.70400	144.43750	2,218	1 s	JAMS
KPG2	OBP	42.23650	144.84540	2,210	1 s	JAMS
HPG1	OBP	35.00300	139.22470	1,176	1 s	JAMS
MPG1	OBP	32.39070	134.47530	2,308	1 s	JAMS
MPG2	OBP	32.64310	134.36470	1,507	1 s	JAMS
DART21418	OBP	38.71056	148.69361	5,662	15 s / 1 min	NOAA
DART21401	OBP	42.61667	152.58333	**5,302**	15 s / 1 min	NOAA
DART21419	OBP	44.45500	155.73556	5,318	15 s / 1 min	NOAA
DART21413	OBP	30.51528	152.11694	5,822	15 s / 1 min	NOAA
Iwate N	GPS	40.11667	142.06667	125.0	5 s	NOW
Iwate M	GPS	39.62722	142.18667	200.0	5 s	NOW
Iwate S	GPS	39.25861	142.09694	204.0	5 s	NOW
Miyagi N	GPS	38.85778	141.89444	160.0	5 s	NOW
Miyagi M	GPS	38.23250	141.68361	144.0	5 s	NOW
Fukushima	GPS	36.97139	141.18556	137.0	5 s	NOW
Omaezaki	GPS	34.40333	138.27500	120.0	5 s	NOW
Mie Owase	GPS	33.90222	136.25944	210.0	5 s	NOW
Wakayama SW	GPS	33.64222	135.15667	201.0	5 s	NOW
Tokushima Kaiyo	GPS	33.46056	134.49667	430.0	5 s	NOW
Hanasaki	Tide	43.28333	145.56667	C	15 s	JMA
Kiritappu Port	Tide	43.07833	145.11639	C	5 s	NOW
Kushiro	Tide	42.98333	144.36667	C	15 s	JMA
Kushiro Port	Wave	42.91056	144.39722	50.0	5 s	NOW
Tokachi	Wave	42.65167	143.68556	23.0	5 s	NOW
Tomakomai West Port	Tide	42.62972	141.62111	C	5 s	NOW
Tomakomai Port	Wave	42.54389	141.44583	50.7	5 s	NOW
Shiraoi Port	Tide	42.52139	141.32056	C	5 s	NOW
Muroran Port	Tide	42.34444	140.95333	C	5 s	NOW

Mutsuogawara Port	Tide	40.92639	141.38722	C	5 s	NOW
Mutsuogawara Port	Wave	40.92500	141.42417	43.8	5 s	NOW
Hachinohe	Tide	40.53333	141.53333	C	15 s	JMA
Hachinohe Port	Tide	40.53306	141.55556	C	5 s	NOW
Hachinohe Port	Wave	40.56083	141.56833	27.7	5 s	NOW
Kuji Port	Tide	40.19222	141.79667	C	5 s	NOW
Kuji Port	Wave	40.21778	141.86000	49.5	5 s	NOW
Miyako	Tide	39.65000	141.98333	C	G	JMA
Kamaishi	Tide	39.27056	141.89278	C	30 s	JCG
Ofunato	Tide	39.01667	141.75000	C	G	JMA
Onagawa	Tide	38.40142	141.50494	C	1 min	THEP
Ayukawa	Tide	38.30000	141.50000	C	G	JMA
Sendai New Port	Wave	38.25000	141.06611	21.3	5 s	NOW
Soma	Tide	37.83333	140.96667	C	G	JMA
Fukushima-1	Wave	37.41402	141.05193	C	0.5 s	TEP
Onahama	Tide	36.93333	140.90000	C	15 s	JMA
Tokai	Tide	36.46407	140.61706	C	0.5 s	JAPC
Choshi	Tide	35.75000	140.86667	C	15 s	JMA
Kozushima	Tide	34.20500	139.13667	C	30 s	JCG
Miyakejima	Tide	34.06389	139.48389	C	30 s	JCG
Miyakejima Tsubota	Tide	34.05000	139.55000	C	15 s	JMA
Hachijojima	Tide	33.12667	139.80778	C	30 s	JCG
Chichijima	Tide	27.10000	142.20000	C	15 s	JMA

* OBP: Ocean Bottom Pressure gauge, GPS: GPS wave gauge, Tide: Tide gauge, Wave: Wave gauge.
† Water depth written in bold was read from the bathymetry grid data. Others are referred from station lists provided by the agencies. C: Coastal point. ‡ Sampling interval of digital sea-level data provided by the agencies. G: Graphic data of sea-level change, which were published by JMA, were digitized for this study. § Agencies or networks which are responsible for the sea-level data
ERI: Earthquake Research Institute, Univ. of Tokyo, JAMS: Japan Agency for Marine-Earth Science and Technology (JAMSTEC), NOAA: National Oceanic and Atmospheric Administration, USA, NOW: Nationwide Ocean Wave information network for Ports and HArbourS (NOWPHAS), JMA: Japan Meteorological Agency, JCG: Japan Coastal Guard, THEP: Tohoku Electric Power Company, TEP: Tokyo Electric Power Company, JAPC: Japan Atomic Power Company

778 Table 2. Inversion result for five time windows at each subfault

No.	Lat.(°N) *	Lon.(°E) *	Tr (min) †	S1 (m) ‡	S2 (m) ‡	S3 (m) ‡	S4 (m) ‡	S5 (m) ‡	Total slip (m)
0A	40.198	144.35	1.783	0	0	2.77	6.57	1.36	10.70
0B	39.738	144.331	1.400	3.4	1.17	1.09	0	14.83	20.49
0C	39.3	144.2	1.042	0.69	3.64	6.58	11.01	14.17	36.08
0D	38.862	144.069	0.658	2.66	2.61	11.08	0.16	14.14	30.65
0E	38.424	143.939	0.625	8.22	4.42	12.62	3.89	22.73	51.89
0F	37.986	143.81	0.625	14.79	4.04	23	4.13	23.18	69.14
0G	37.547	143.682	0.658	6.65	3.56	0	0	21.5	31.72
0H	37.135	143.4	1.042	9.89	4.28	7.47	0.82	0	22.45
0I	36.73	143.07	1.317	0	0	0.09	0.66	0	0.76
0J	36.325	142.74	1.667	0	0	0	0	4.33	4.33
0K	35.905	142.504	2.083	0	0	0	2	3.91	5.90
1A	40.24809	144.06599	1.717	0	0	0	0	0.84	0.84
1B	39.78808	144.04888	1.317	1.43	0	0	1.16	0.4	2.98
1C	39.35008	143.91966	0.933	4.79	0	0	0.52	8.39	13.71
1D	38.91208	143.7904	0.592	0.9	6.05	4.21	0	11.26	22.43
1E	38.47408	143.66209	0.417	10.71	3.49	7.87	15.31	0	37.38
1F	38.03608	143.53475	0.417	6.13	0.03	8.78	0	0	14.93
1G	37.59708	143.40839	0.592	11.11	0	2.27	0	5.74	19.13
1H	37.18508	143.12788	0.933	10.11	0	0	0	0	10.11
1I	36.78008	142.79933	1.250	0	0	0	0	0	0
1J	36.37508	142.47074	1.667	0	0	0	0	1.83	1.83
1K	35.95508	142.23617	2.083	0	1.12	0	0	1.41	2.53
2A	40.29817	143.78198	1.667	0	0	0	0	1.34	1.34
2B	39.83817	143.76677	1.250	0	0	0.23	0	0	0.23
2C	39.40017	143.63932	0.833	2.47	1.26	0	0	2.92	6.65
2D	38.96217	143.5118	0.417	1.12	1.23	4.11	4.89	5.55	16.90
2E	38.52417	143.38519	0.000	0	0	14.15	0	12.41	26.55
2F	38.08617	143.25951	0.000	2.85	8.21	0	11.96	1.66	24.67
2G	37.64717	143.13478	0.417	1.87	8.45	0	0	7.74	18.06
2H	37.23517	142.85576	0.833	4.83	0	0	0	0	4.83
2I	36.83017	142.52866	1.250	0	0	0	0	0	0
2J	36.42517	142.20148	1.667	0	0	0	0	0.61	0.61

2K	36.00517	141.96835	2.083	0	0	0	0	2.35	2.35
3A	40.39778	143.21625	1.667	0.65	0	0	0	0	0.65
3B	39.93778	143.20484	1.250	0	0	0	0	1.06	1.06
3C	39.49978	143.08095	0.833	0	0	0	0	0	0
3D	39.06178	142.95688	0.417	0	0	0	8.63	4.51	13.14
3E	38.62378	142.83367	0.000	0	0	0	0	15.55	15.55
3F	38.18578	142.71131	0.000	0	0	0	10.76	10.82	21.58
3G	37.74678	142.58984	0.417	0	0	0	1.57	9.3	10.87
3H	37.33478	142.31381	0.833	10.53	0	0	0	0	10.53
3I	36.92978	141.98959	1.317	2.12	0	0	0	0	2.12
3J	36.52478	141.66523	1.717	0	0	0	0	0.08	0.08
3K	36.10478	141.43498	2.125	0	0	0	0	1.97	1.97
4A	40.49672	142.65351	1.717	0.82	0	0	0	0	0.82
4B	40.03672	142.64591	1.317	0	0	0	0	0	0
4C	39.59872	142.52555	0.933	0	0	0	0	0	0
4D	39.16072	142.40494	0.592	0	0	0	0	2.81	2.81
4E	38.72272	142.28513	0.417	0	0	0.58	0	1.83	2.41
4F	38.28472	142.16607	0.417	8.37	0	0	0	5.89	14.26
4G	37.84572	142.04786	0.592	0	0	0	0.09	2.58	2.67
4H	37.43372	141.77481	0.933	4.47	0	0	0	0	4.47
4I	37.02872	141.45347	1.500	0	0	0	0	0	0
4J	36.62372	141.13193	1.867	0	0	0	0	2.75	2.75
4K	36.20372	140.90455	2.242	0	0	0	0	2.55	2.55

Location (latitude [Lat.] and longitude [Lon.]) indicates the northeast corner of each subfault. The fault length: 50 km, the strike: 193º, the slip angle: 81º are common to all the subfaults. The widths are 25 km for subfaults 0 and 1*, 50 km for the other subfaults. The dip angles are 8 º for subfaults 0* and 1*, 10 º, 12 º, and 16 º for subfaults 2*, 3* and 4*, respectively. The top depths are 0 km, 3.5 km, 7 km, 15.6 km and 26 km, beneath seafloor, for subfaults 0*, 1*, 2*, 3* and 4*, respectively. † Arrival time (Tr) of rupture front at an edge or a corner of subfault assuming a rupture velocity of 2.0 km/s. ‡ S1: Slip during the time from Tr to $Tr+\Delta t$. Here, Δt of 0.5 min is a rise time of slip for each time window. S2: Slip during the time from $Tr+\Delta t$ to $Tr+2\Delta t$. S3: Slip during the time from $Tr+2\Delta t$ to $Tr+3\Delta t$. S4: Slip during the time from $Tr+3\Delta t$ to $Tr+4\Delta t$. S5: Slip during the time from $Tr+4\Delta t$ to $Tr+5\Delta t$.

Figure Captions

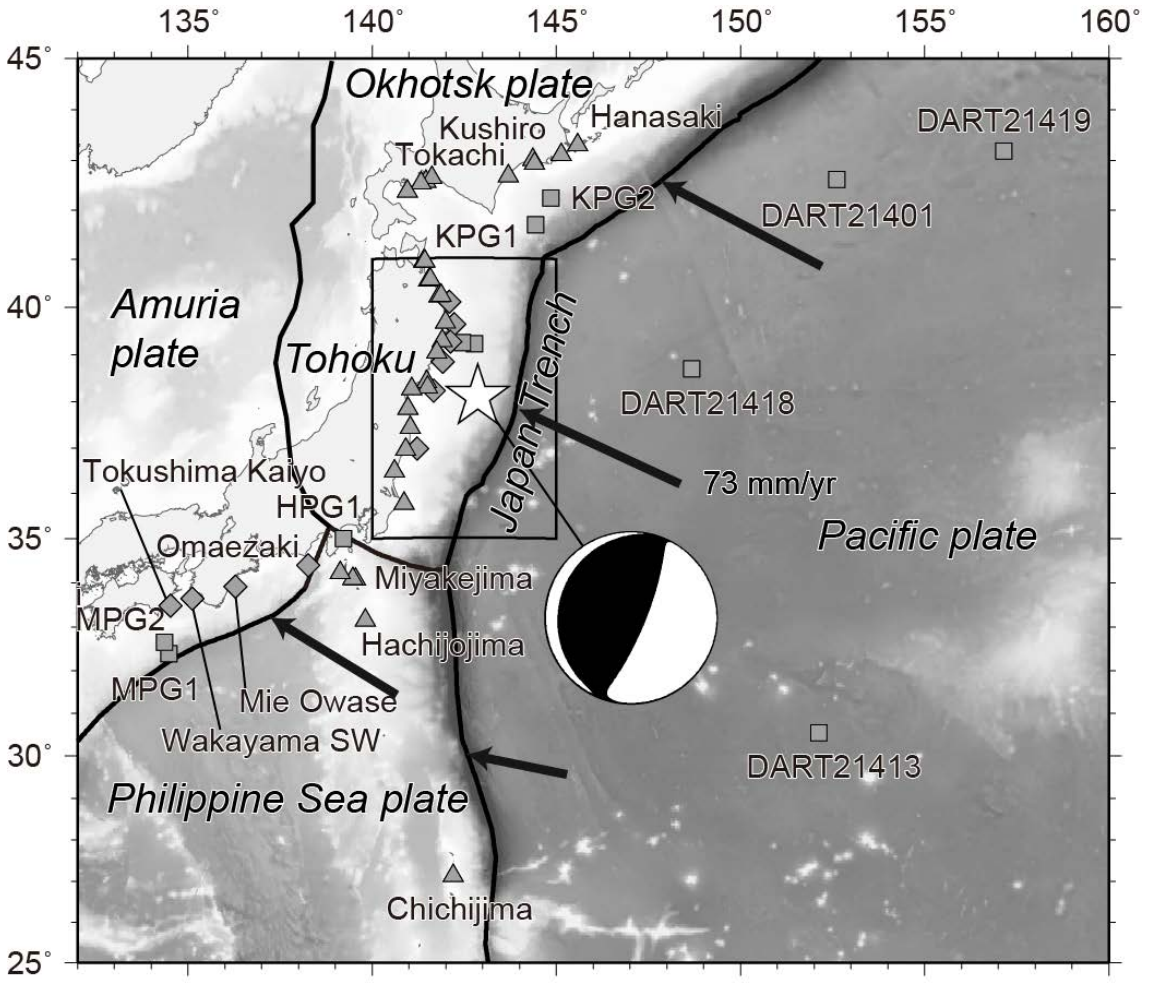

792

793 **Figure 1.** Epicenter of the 2011 Tohoku earthquake (white star), W-phase moment
794 tensor solution by USGS, and stations that recorded the tsunami. Squares,
795 diamonds and triangles indicate Ocean Bottom Pressure (OBP) gauges, GPS wave
796 gauges, and coastal tide or wave gauges, respectively. Thin rectangle indicates the
797 region shown in Figure 2. Black arrows indicate relative plate motions of the plates
798 based on REVEL model (Sella *et al.*, 2002).

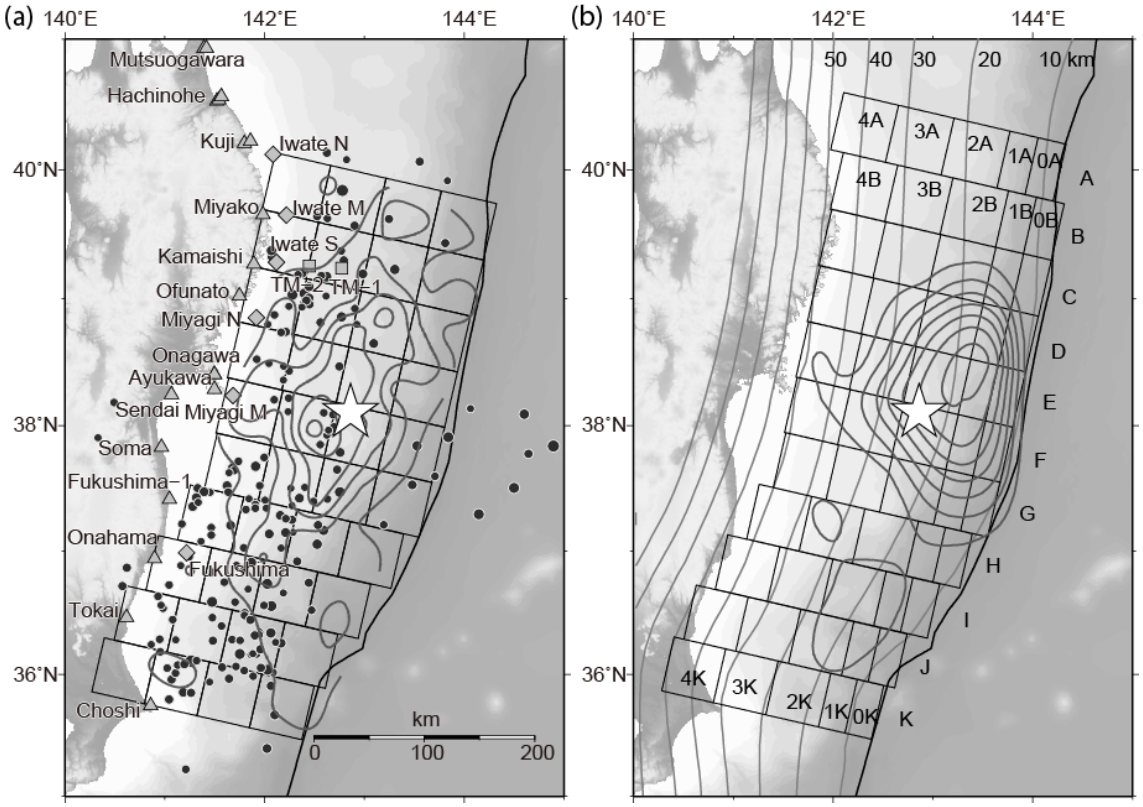

Figure 2. Subfaults and slip distribution of the 2011 Tohoku earthquake. **(a)** Locations of 40 subfaults used by Fujii *et al.* (2011) and the slip distribution with 5 m contour interval estimated from strong-motion data (Yokota *et al.*, 2011). **(b)** the 55-subfault model used in this study and the slip distribution with 8 m contour interval estimated from GPS and acoustic data (Geospatial Information Authority of Japan (GSI), 2011). Aftershocks within 1 day located by JMA (solid circles) and the locations of OBP gauges (squares), GPS wave gauges (diamonds) and coastal tide or wave gauges (triangles) are shown in **(a).** The depths to the upper surface of the Pacific plate (Nakajima and Hasegawa, 2006) are shown in **(b).**

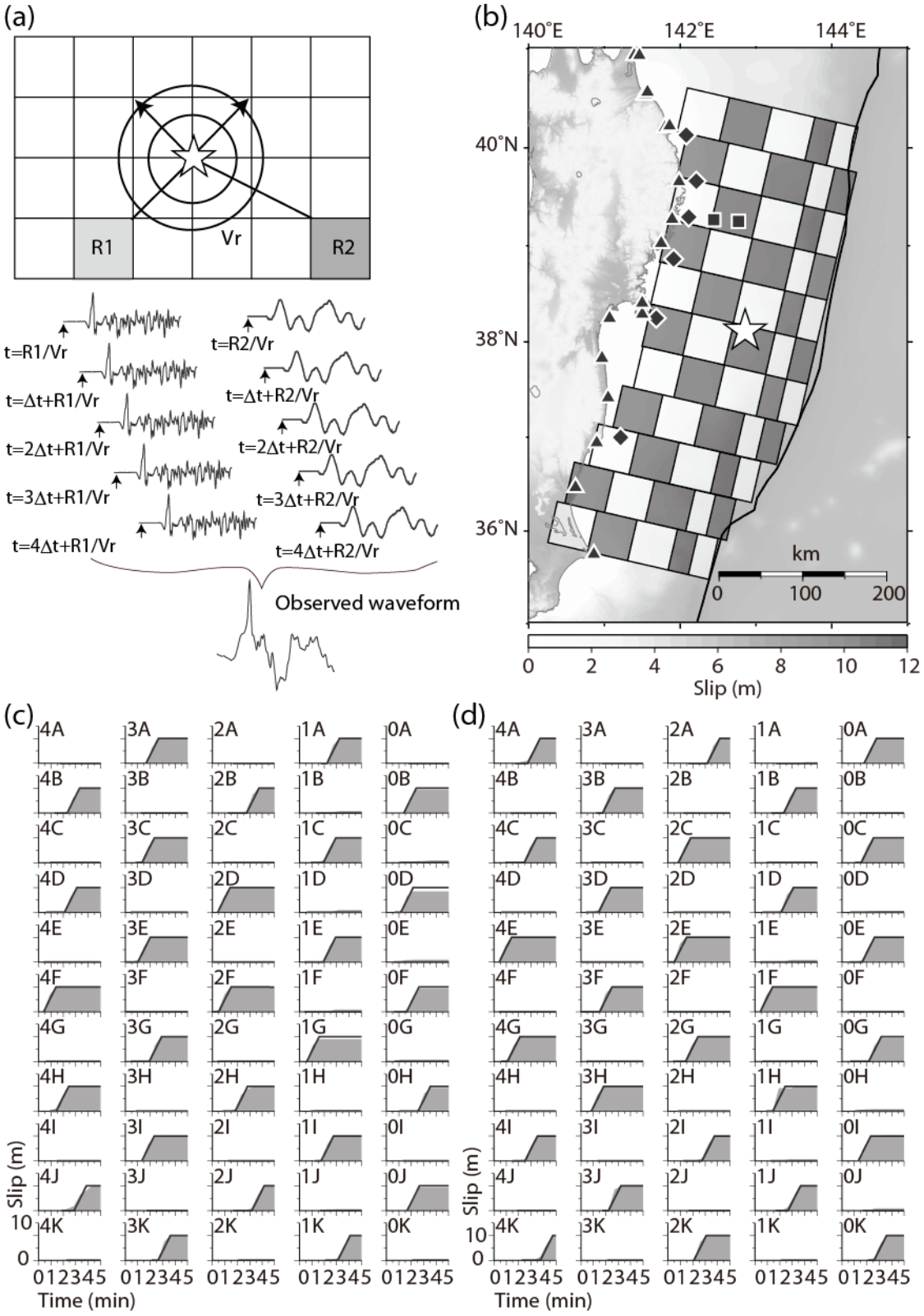

Figure 3. (a) Schematic figure showing multiple time-window inversion. Tsunami waveforms at each station are computed from each subfault, and shifted by Δt (30 s

812 in this study) and used as the Green's functions for the inversion. The start time of
813 the first Green's function is set at onset of rupture from the epicenter assuming a
814 rupture velocity (Vr = 2.0 km/s). (b) Assumed slip distribution (gray color: 10 m, and
815 white color: 0 m) on subfaults for the checker-board test. The test reproduced the
816 same spatial distribution. The locations of the stations and the epicenter (see Figure
817 2) are also shown. (c) Temporal changes of slip distribution on 55 subfaults for the
818 checker-board test. Solid curves indicate assumed slip history (10 m slip is reached
819 in 60 s at alternate subfaults). The gray blocks show estimated slip histories. They
820 are almost identical. (d) Temporal changes of slip distribution for the
821 complementary slip distribution to (b) or (c).
822

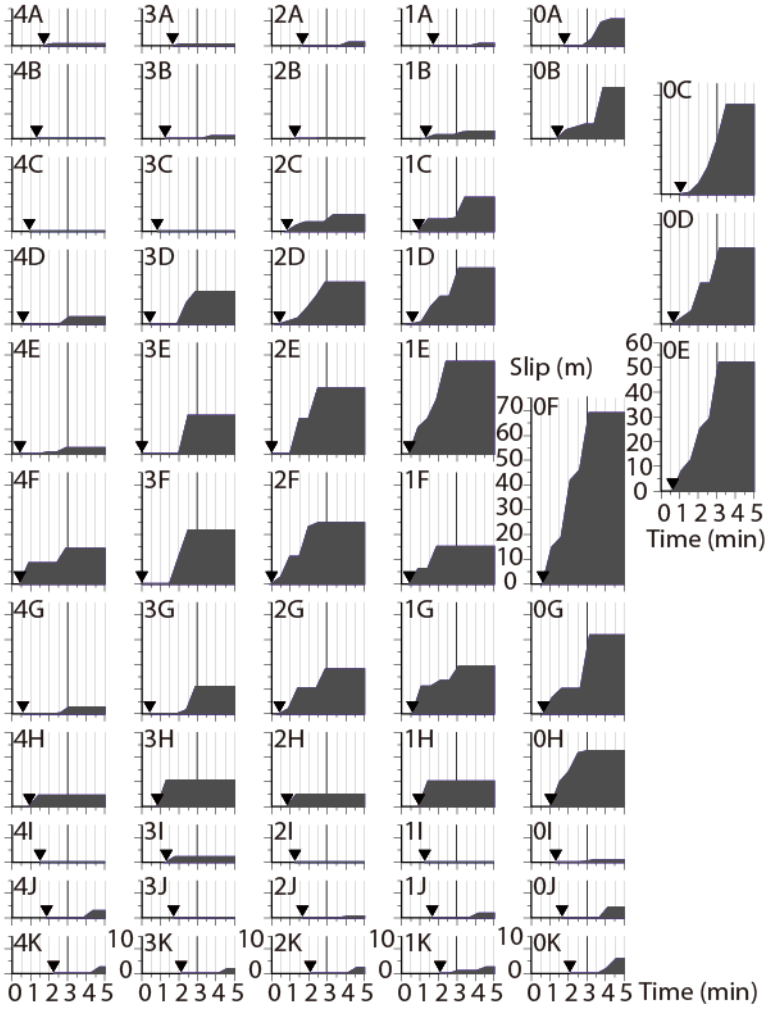

Figure 4. Spatial and temporal distribution of slip on 55 subfaults. Temporal changes of slip after the rupture onset (inverse triangles, assuming a rupture velocity of 2.0 km/s) with 30 s interval are estimated. Rise time for each time window is assumed to be 30 s. Thick vertical bars indicate 3 min after the earthquake origin time.

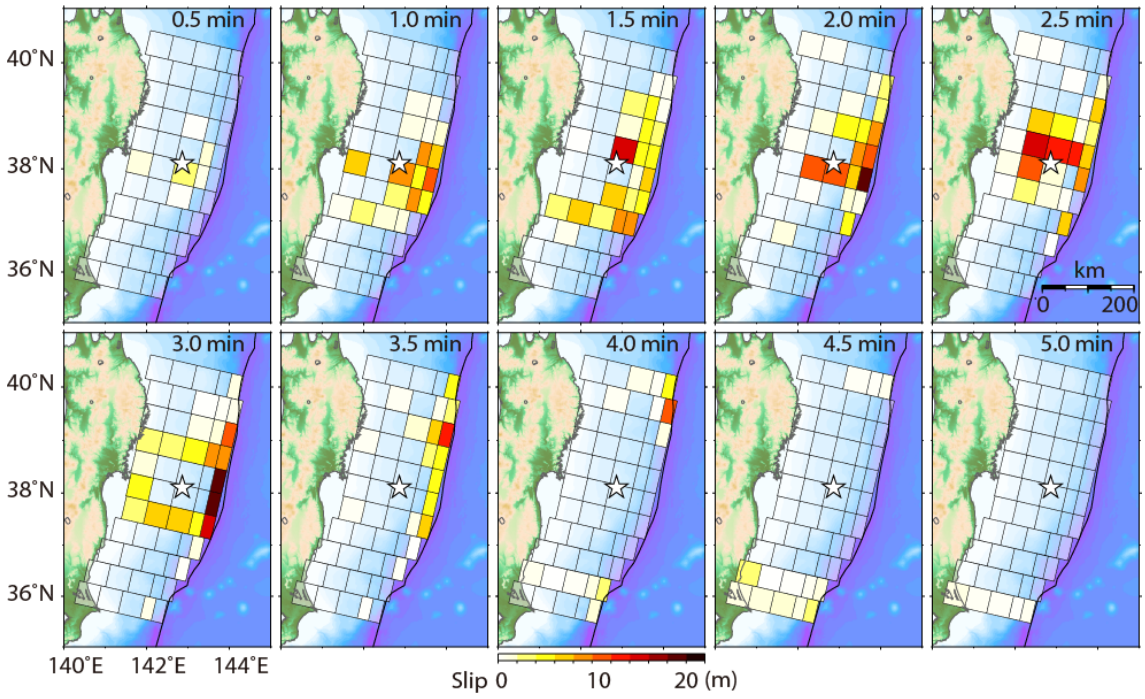

830

831 **Figure 5.** Snapshot of slip on subfaults at 30 s interval. The slip at each 30 s is
832 estimated from the interpolation of the values in Figure 4. The white star
833 represents the epicenter, where the rupture is assumed to start.

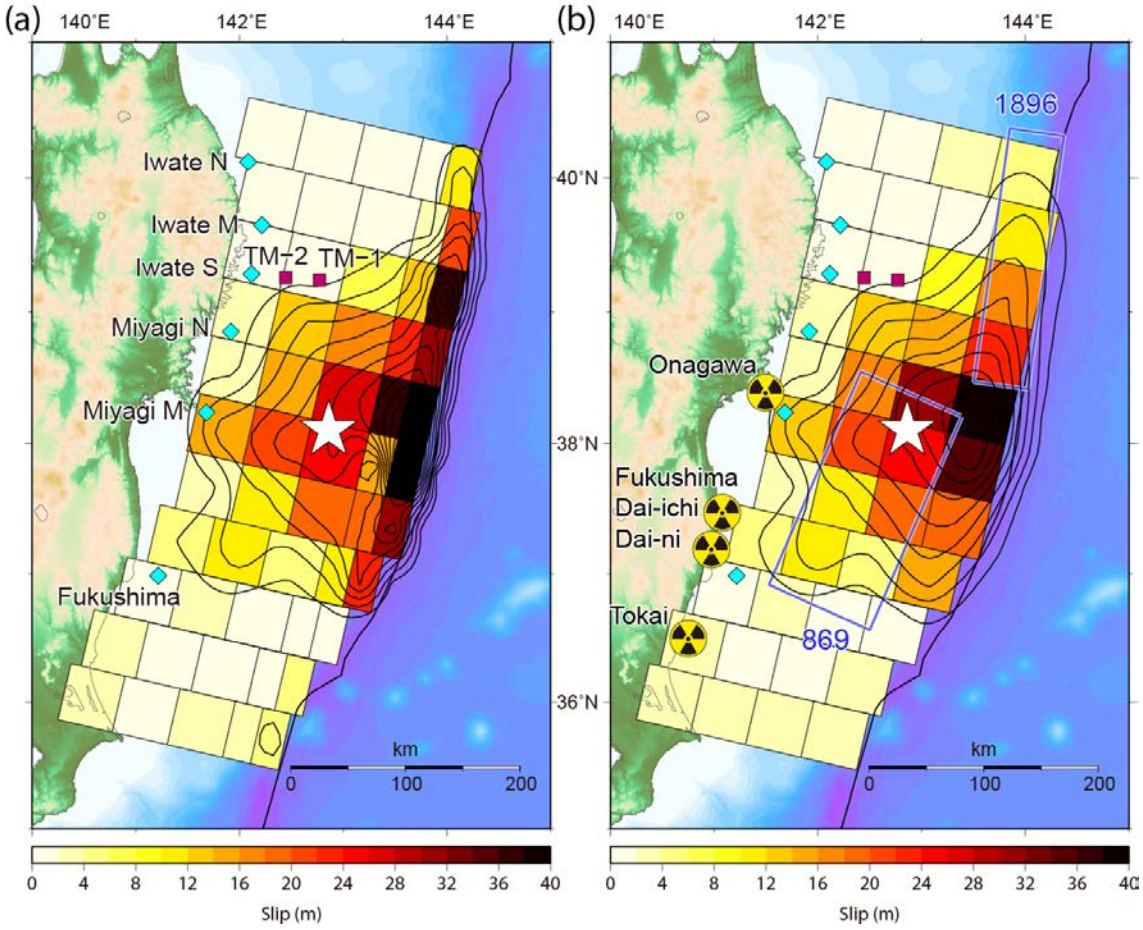

834

835 **Figure 6.** Final or cumulative slip distribution on 55 subfaults (a) and 44 subfaults
836 (b). The contour interval is 4 m. The white star indicates the epicenter. The OBP
837 and GPS wave gauges in the source areas are also shown in a. The fault models of
838 the 1896 Sanriku earthquake (Tanioka and Satake, 1996a; Tanioka and Seno, 2001)
839 and the 869 Jogan earthquake (Satake *et al.*, 2008a; Namegaya *et al.*, 2010) are
840 shown in (b). Locations of four nuclear power stations (NPS) around the source area
841 are also shown.

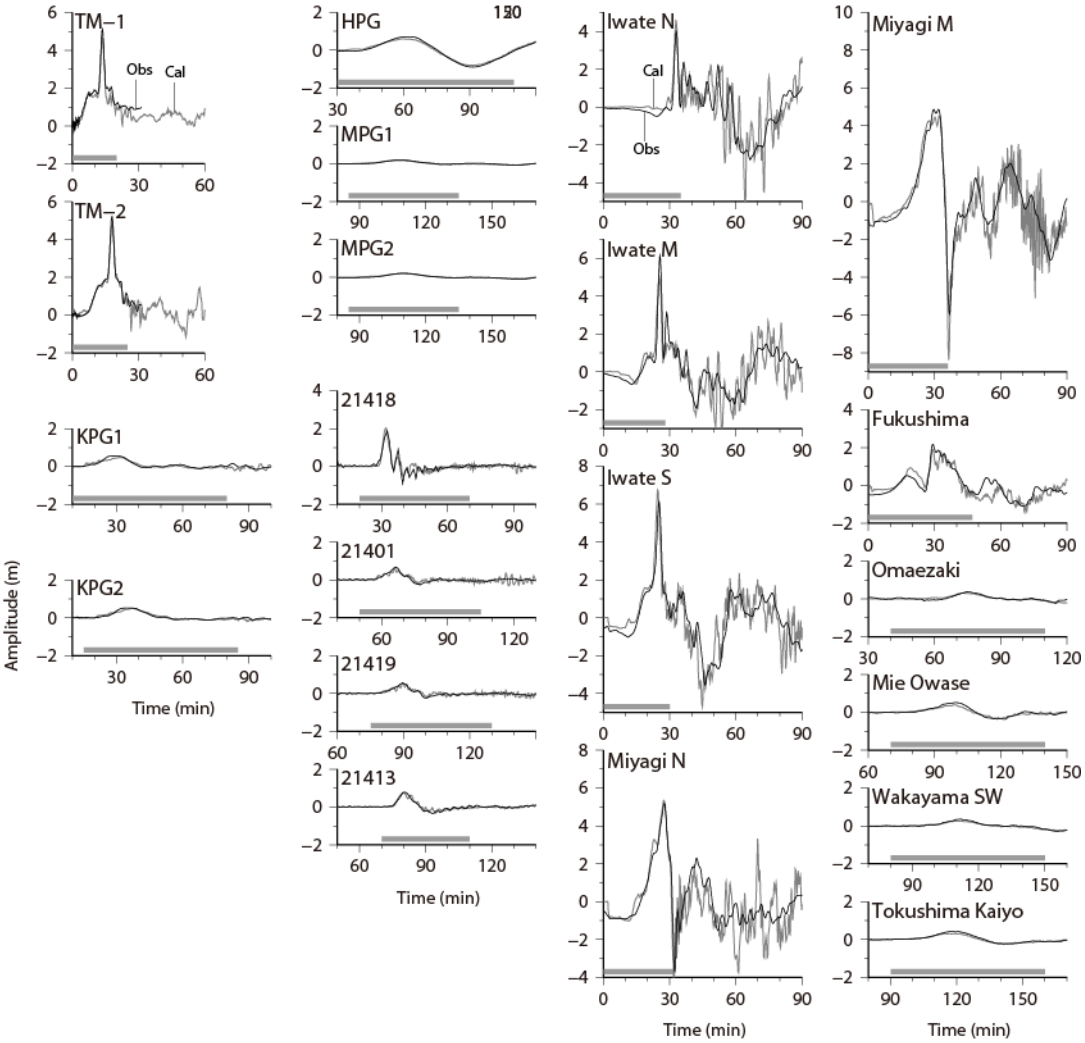

842

843 **Figure 7 (a).** The observed (solid curves) and computed (gray curves) tsunami
844 waveforms at OBP and GPS gauges. Time is measured from the earthquake origin
845 time. The gray bars above the time axis indicate time ranges for the inversion.

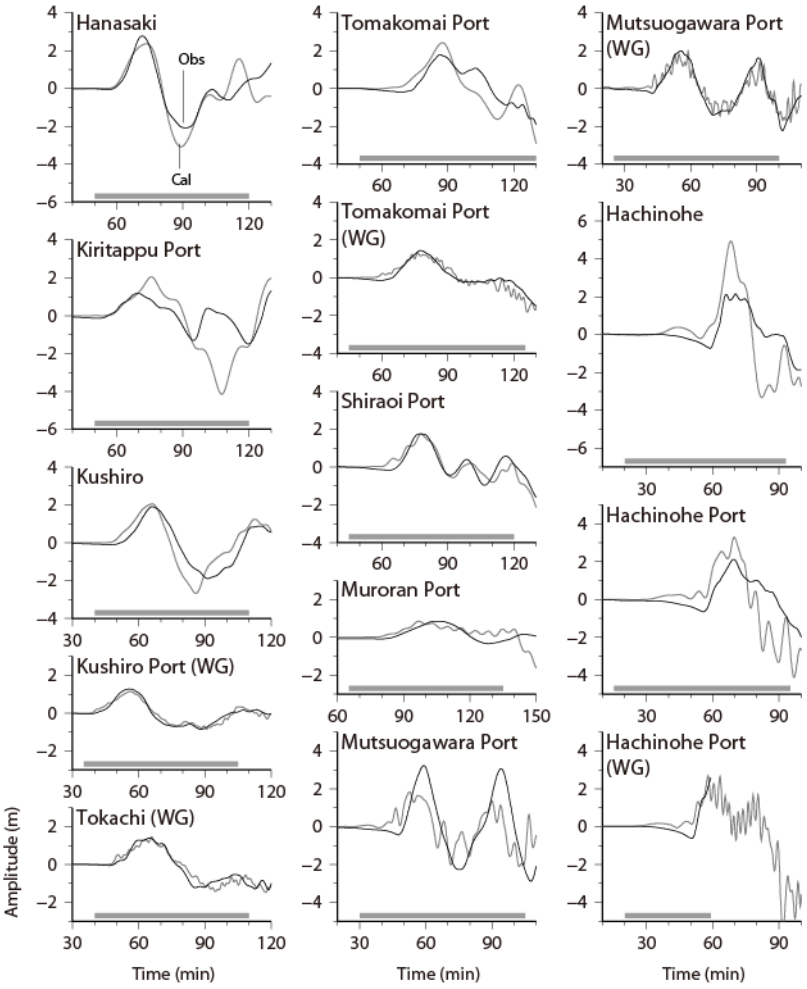

846

847 **Figure 7 (b).** Same as Figure 7 (a) for the wave and tide gauges.

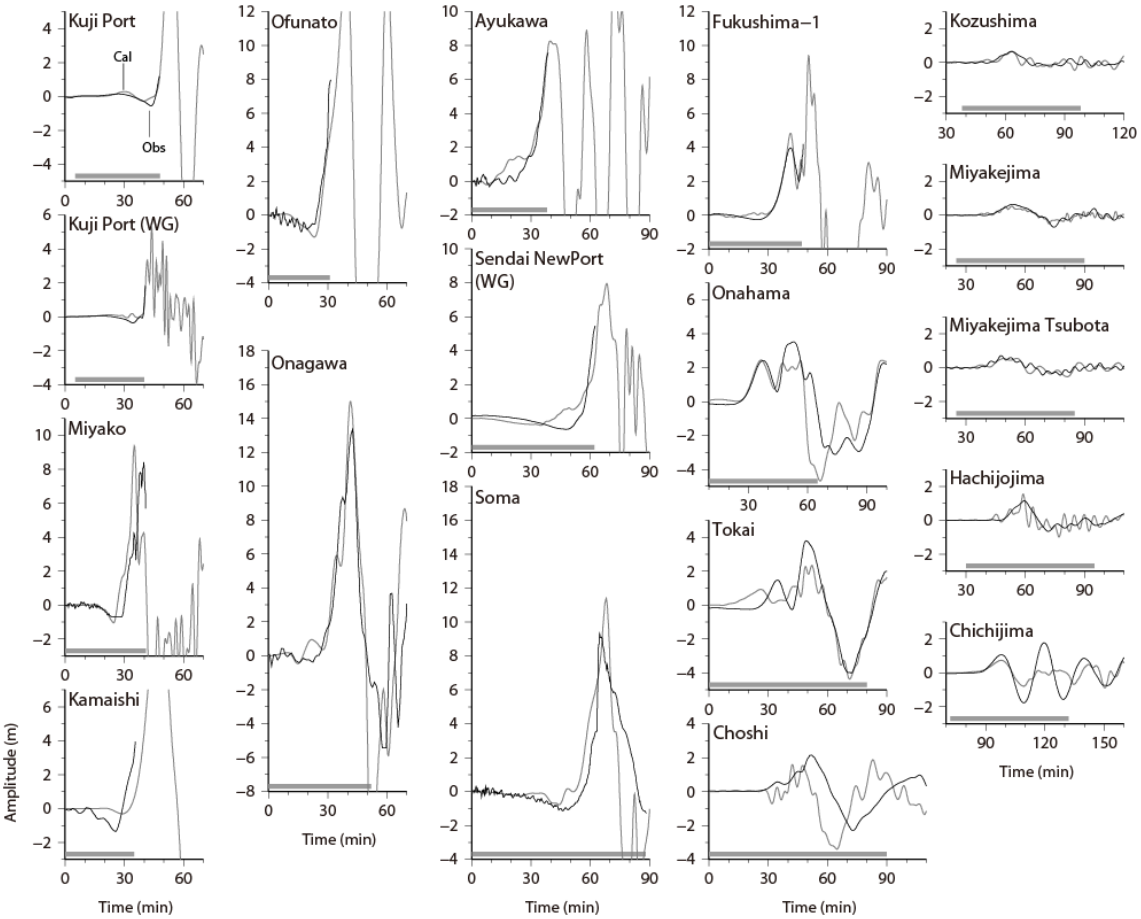

848

849 **Figure 7 (c)**. Same as Figure 7 (b).

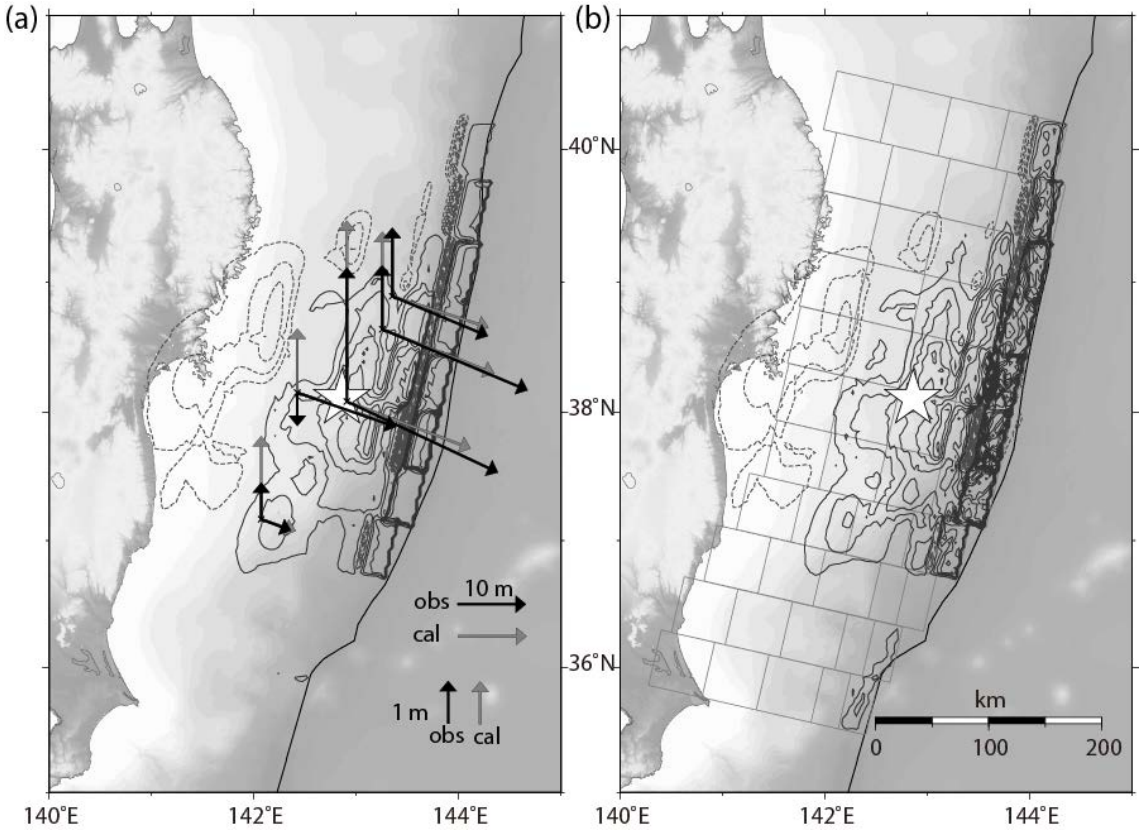

850

851 **Figure 8.** Seafloor displacement computed from the estimated slip distribution
852 (Table 2 and Figure 6a). **(a)** Vertical displacement of ocean floor is shown with
853 contours (solid: uplift with 1 m interval; dashed: subsidence with 0.5 m interval).
854 The horizontal and vertical displacements at GPS/A locations (Sato *et al.*, 2011) are
855 also compared (black: observed, gray: computed). (b) The effect of horizontal
856 movement and ocean floor slope is included by the method of Tanioka and Satake
857 (1996b).

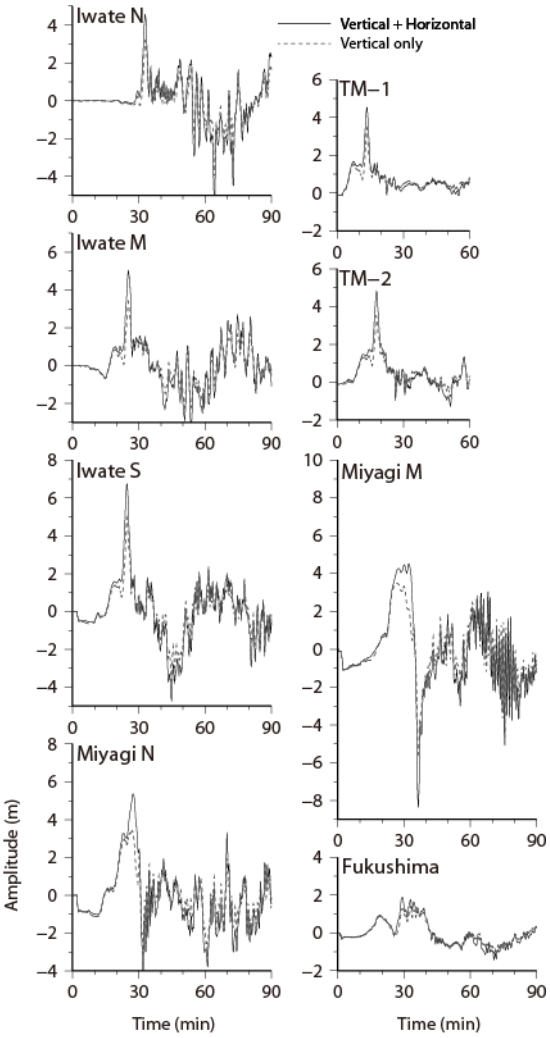

858

859 **Figure 9.** Computed tsunami waveforms at selected OBP gauge and GPS wave
860 gauge stations by including the effects of horizontal components (solid curves) and
861 from only vertical displacements (dashed curves).

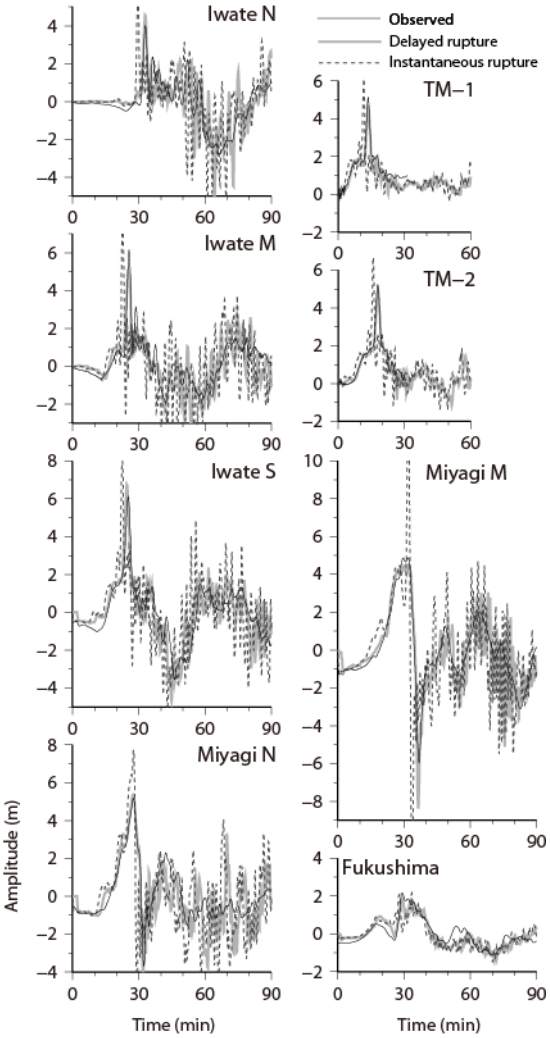

862

863 **Figure 10.** Computed tsunami waveforms at selected OBP gauge and GPS wave
864 gauge stations from delayed slip, or the results of multiple time-window analysis
865 (gray curves) and from the final slip distribution assuming instantaneous rupture
866 (dashed curves) compared with the observations (solid curves).

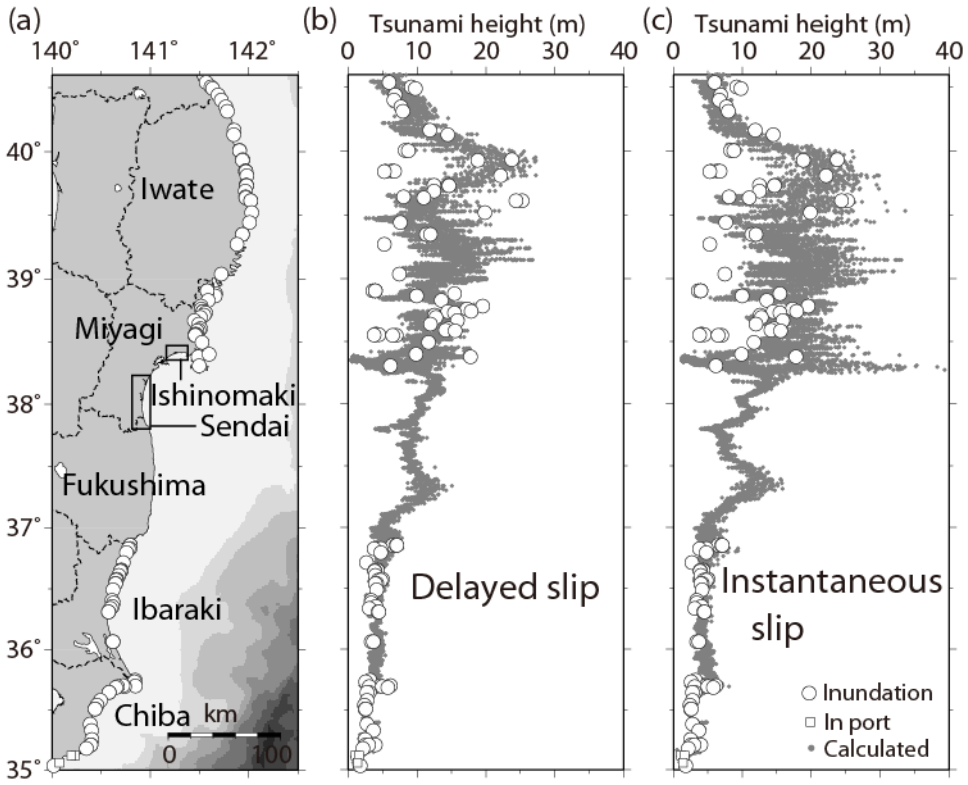

867

868 **Figure 11**. Coastal tsunami heights computed from delayed slip (**b**) and
869 instantaneous slip (**c**), compared with the measured tsunami heights whose
870 locations are shown in (**a**): inundation heights (circles) and tsunami heights in port
871 (squares) (Tsuji *et al.*, 2011). The rectangles in the map (**a**) show the area for
872 inundation computations (Figures 13 and 14)

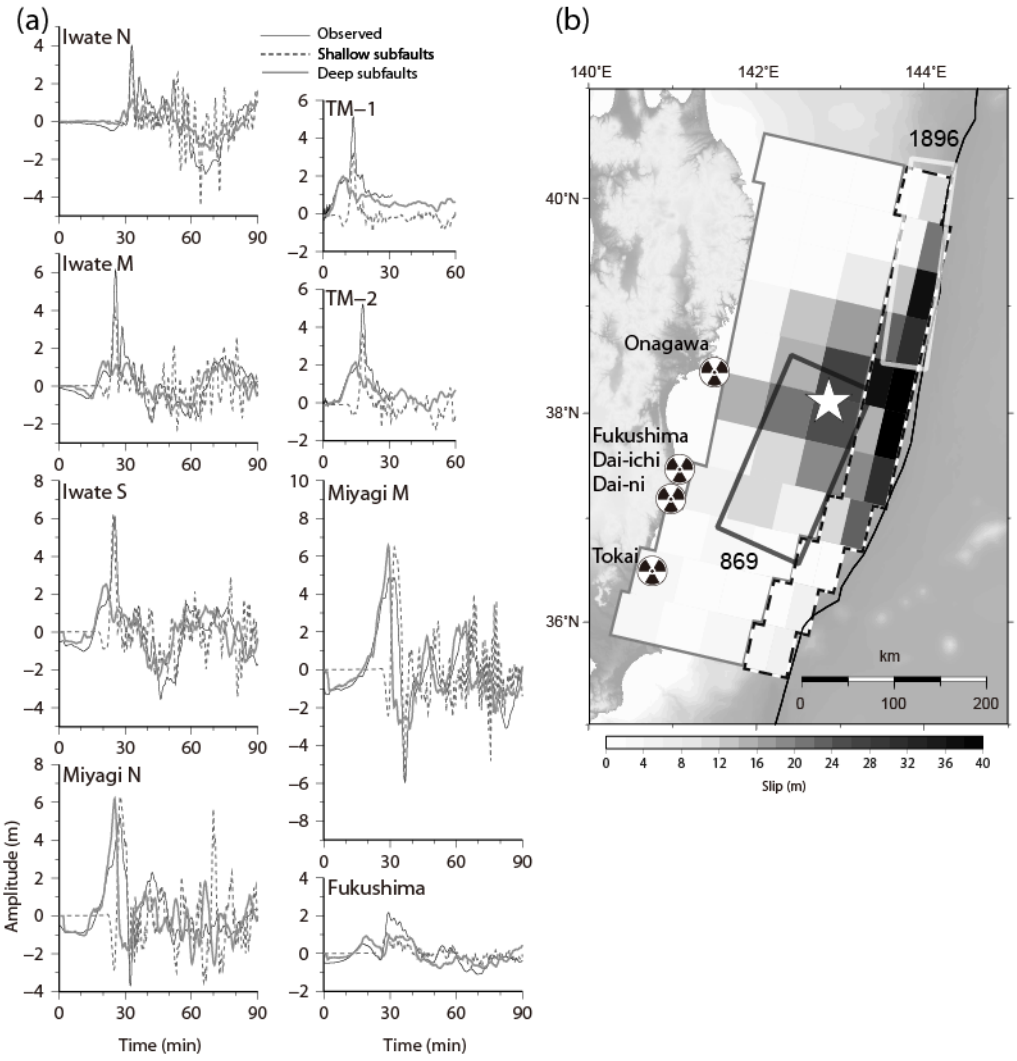

873

874 **Figure 12**. **(a)** The tsunami waveforms computed from deep subfaults (gray curves)
875 and the shallow subfaults (dashed curves) compared with the observed waveforms
876 (solid curves). **(b)** the slip distribution of this study and the previous models (thick
877 rectangles) of the 1896 Sanriku tsunami earthquake (Tanioka and Satake, 1996a;
878 Tanioka and Seno, 2001) and the 869 Jogan earthquake (Satake *et al.*, 2008a;
879 Namegaya *et al.*, 2010). The locations of four NPBs are also shown.

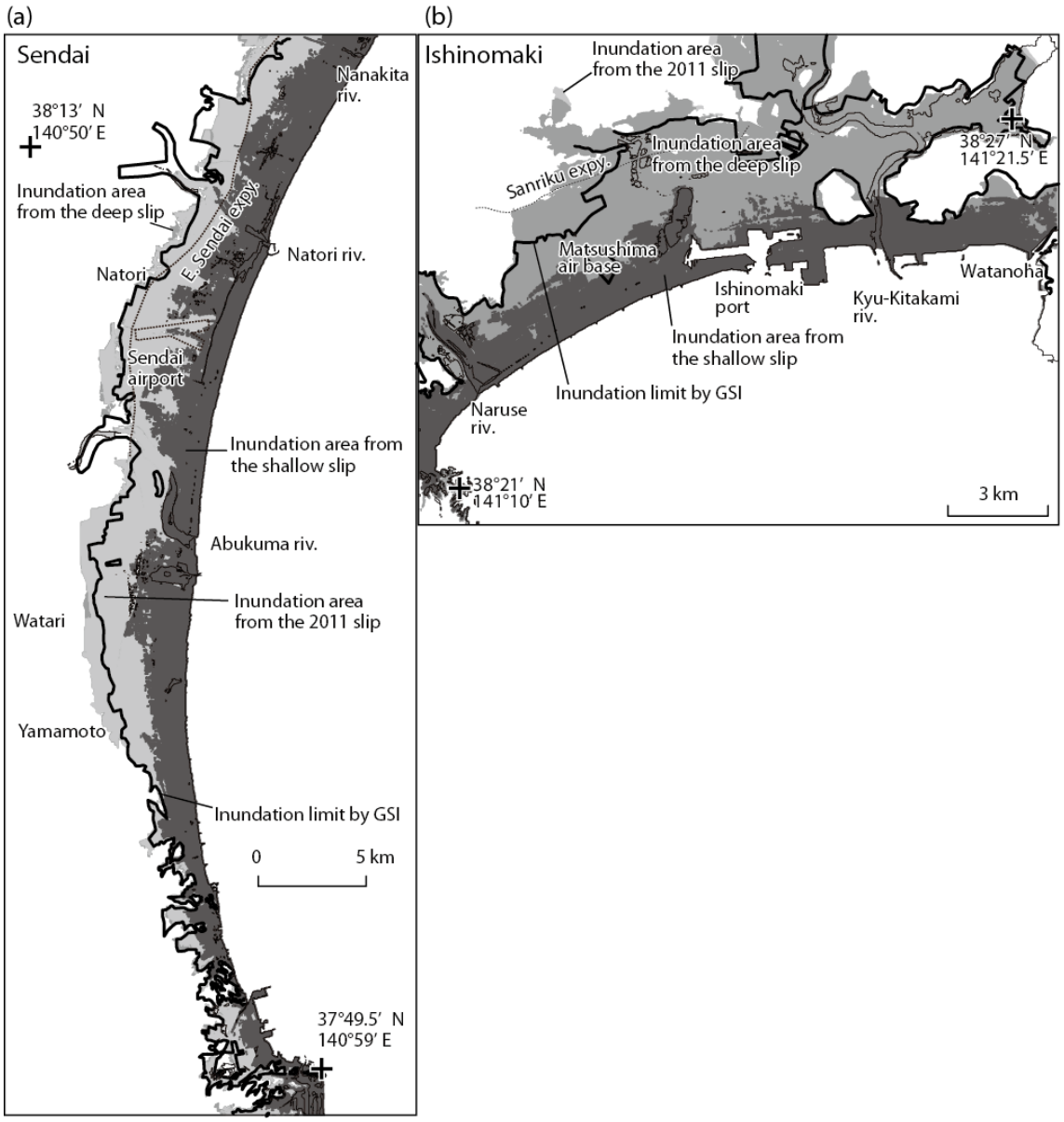

880

881 **Figure 13**. The computed tsunami inundation areas in Sendai (**a**) and Ishinomaki
882 (**b**) plains from the deep, shallow and composite (the 2011) slips. The inundation
883 area is defined as the land grids where the flow depth is more than 0.5 m. The
884 inundation areas from the deep slip (gray) and the 2011 slip (lighter gray) models
885 are almost identical, whereas the inundation area from the shallow slip (darker
886 gray) is much smaller than these. Also shown by thick solid curves are the observed
887 tsunami inundation areas estimated by GSI (Nakajima and Koarai, 2011).

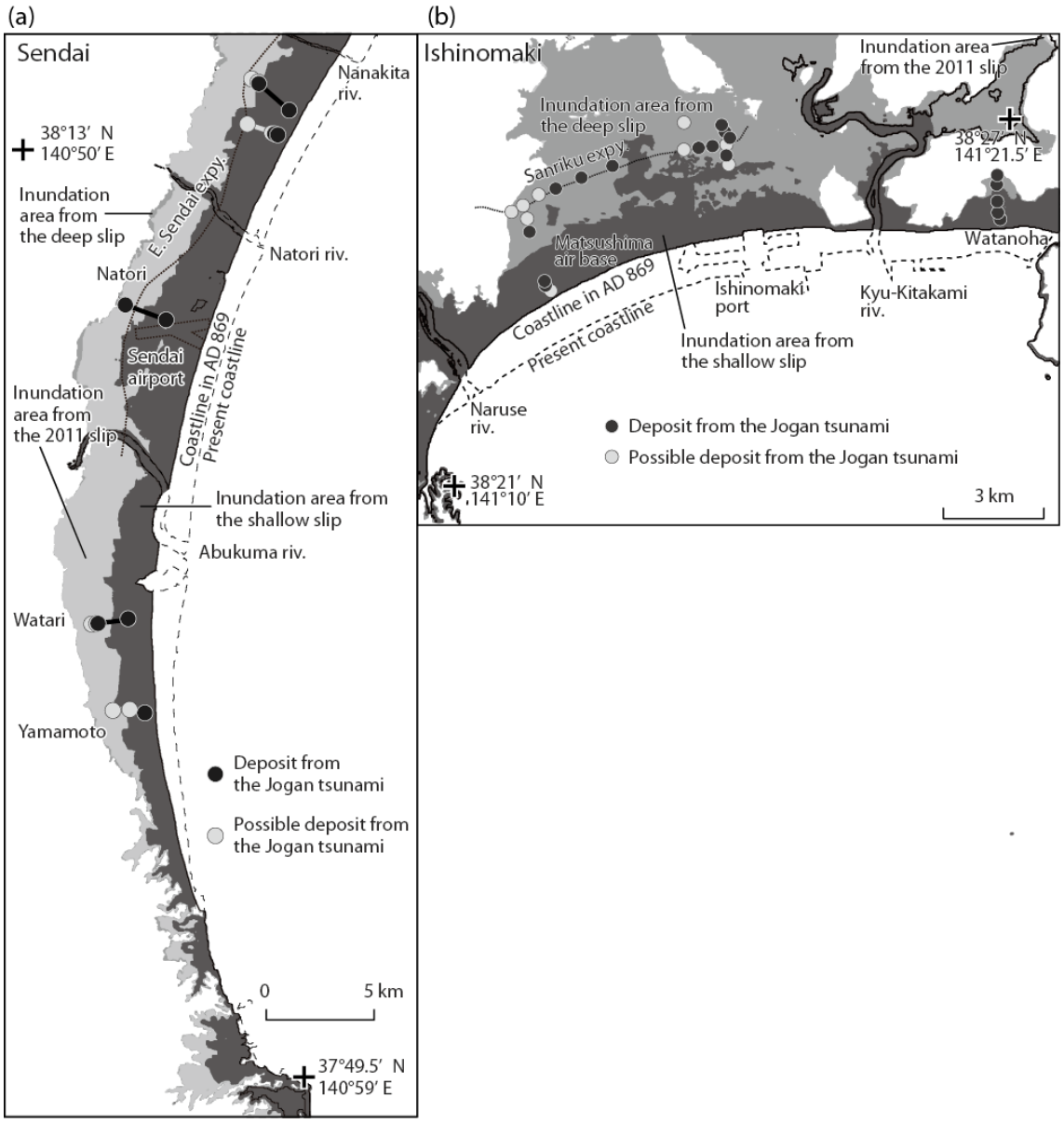

888

889 **Figure 14**. Same as Figure 13, but a reconstructed bathymetry and topography at
890 the time of the 869 earthquake was used for tsunami inundation simulations. Also
891 shown by circles are the distributions of the 869 tsunami deposits (Sawai *et al.*,
892 2007; Shishikura *et al.*, 2007; Sawai *et al.*, 2008b).

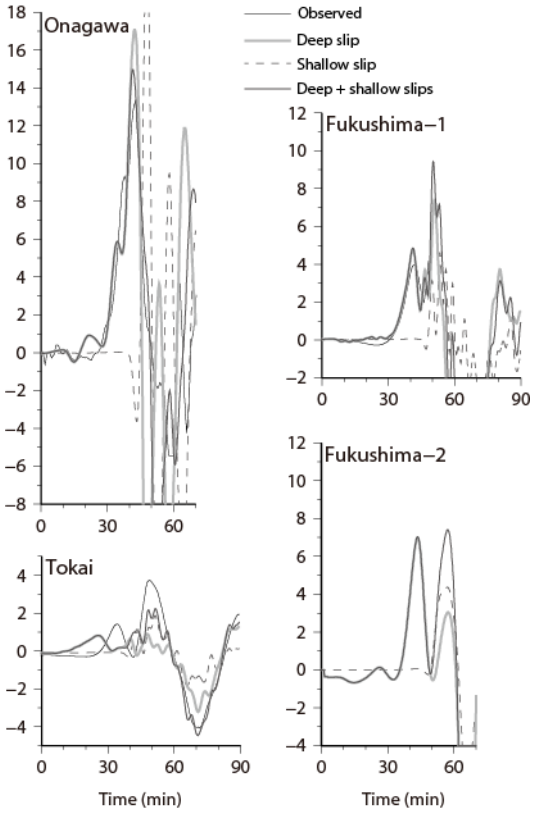

893

894 **Figure 15.** Comparison of tsunami waveforms computed near the four NPSs from
895 deep slip (gray curves), shallow slip (dashed curves) and composite or the 2011
896 source (solid curves) with the observations (thick curves in gray).

897